Producing a compound Nucleus via Inelastic Scattering: The 90Zr(alpha,alpha')90Zr* Case

J. E. Escher, F. S. Dietrich

May 30, 2008

Disclaimer

This document was prepared as an account of work sponsored by an agency of the United States government. Neither the United States government nor Lawrence Livermore National Security, LLC, nor any of their employees makes any warranty, expressed or implied, or assumes any legal liability or responsibility for the accuracy, completeness, or usefulness of any information, apparatus, product, or process disclosed, or represents that its use would not infringe privately owned rights. Reference herein to any specific commercial product, process, or service by trade name, trademark, manufacturer, or otherwise does not necessarily constitute or imply its endorsement, recommendation, or favoring by the United States government or Lawrence Livermore National Security, LLC. The views and opinions of authors expressed herein do not necessarily state or reflect those of the United States government or Lawrence Livermore National Security, LLC, and shall not be used for advertising or product endorsement purposes.

Producing a compound nucleus via inelastic scattering: The ^{90}Zr$(\alpha, \alpha')^{90}$Zr* case

Jutta E. Escher and Frank S. Dietrich

Lawrence Livermore National Laboratory, Livermore, CA 94550

May 27, 2008

Abstract

In a Surrogate reaction a compound nucleus is produced via a direct reaction (pickup, stripping, or inelastic scattering). For a proper application of the Surrogate approach it is necessary to predict the resulting angular momentum and parity distribution in the compound nucleus. A model for determining these distributions is developed for the case of inelastic alpha scattering off a spherical nucleus. The focus is on obtaining a first, simple description of the direct-reaction process that produces the compound nucleus and on providing the basis for a more complete treatment of the problem. The approximations employed in the present description are discussed and the extensions required for a more rigorous treatment of the problem are outlined. To illustrate the formalism, an application to ^{90}Zr$(\alpha, \alpha')^{90}$Zr* is presented.

Contents

1 Introduction

The Surrogate nuclear reactions approach, an indirect method for determining cross sections of compound-nuclear reactions that was originally introduced in the 1970s [22, 17], has recently received renewed attention [78, 79, 80, 62, 9, 63, 36, 30, 34, 29, 21, 41, 15, 60, 19, 38, 8, 33, 42, 31, 37]. Both the early and the more recent applications of the method have focused on cross section estimates for neutron-induced fission for actinide targets, although a few experiments have been designed to obtain (n,γ) cross sections for some rare earth and actinide nuclei. As applications to new areas of interest (various types of compound-nucleus reactions, lower energies, new regions of the isotopic chart) are being explored, a more comprehensive treatment of the Surrogate approach becomes necessary in order to examine previously used approximations, to validate the Surrogate approach, and to determine its limitations. In particular, a more realistic theoretical description of the Surrogate mechanism is required.

In the Surrogate approach the compound nucleus (B^*) occurring in the reaction of interest ($a+A \rightarrow B^* \rightarrow c + C$) is produced via an alternative, "Surrogate" reaction ($d + D \rightarrow B^* + b$) and the measured compound-nucleus decay probabilities are combined with the calculated formation cross section for the compound nucleus in the desired reaction to yield the relevant reaction cross section. This approach is particularly valuable when the target of interest, A, is short-lived and a suitable Surrogate reaction involving a stable target D and a stable projectile d can be identified.

The most significant limitation of the method at this time is the fact that the compound-nuclear spin-parity distributions in the desired and Surrogate reactions differ from each other in a manner that is poorly understood (see "spin-parity population mismatch" in Section 1.1). While optical-model calculations provide fairly reliable spin-parity information for the desired reaction, no tools are currently available for formulating accurate predictions of the spin-parity distributions for compound nuclei produced in Surrogate reactions. This situation does not merely reflect an absence of useful reaction codes, but points to an incomplete picture of the reaction mechanisms that produce the compound nucleus in a Surrogate reaction. A significantly improved (qualitative and quantitative) understanding of the underlying processes is required. This includes a description of direct reactions that populate highly-excited, unbound states, the damping of these doorway states into more complicated configurations that lead to a compound nucleus (or non-equilibrium particle emission), the dependence and influence of these processes on angular momentum, parity, and energy, and possible width fluctuation corrections to the standard Hauser-Feshbach-type formalism.

First steps towards predicting the spin-parity population of a compound nucleus produced in a direct reaction were taken by Andersen *et al.* [1], Back *et al.* [5], and, more recently, by Younes and Britt [78, 79]. These authors employed simple transfer calculations to estimate compound-nucleus spin-parity distribution following various stripping reactions on actinide targets. Younes and Britt used the resulting spin-parity distributions to re-analyze Surrogate (t,pf), (^{3}He,df), and (^{3}He,tf) fission-correlation measurements from the 1970s [22, 17] in order to extract (n,f) cross sections. Compared to earlier Surrogate analyses of the data, their estimated (n,f) cross sections showed significantly improved agreement with evaluated results, where available. Their findings underscore the importance of accounting for the spin-parity mismatch between the desired and Surrogate reactions and highlight the need for further development of theories that describe the processes involved in forming a compound nucleus via a direct reaction.

In the present report a model is developed to predict the spin-parity distribution in a compound nucleus produced via inelastic α scattering. The focus here is on obtaining a first, simple description of the direct-reaction process and on providing the basis for a more complete treatment of the problem. For this reason, we outline what a more rigorous treatment of the mechanisms that produce a compound nucleus entails, clearly specify the approximations made in the present description, and provide details about the model and model inputs employed. We discuss an application for inelastic α scattering off the doubly-closed shell nucleus ^{90}Zr, for which much experimental data is available, and provide a first estimate for the compound-nucleus spin-parity distributions produced via inelastic scattering. The resulting cross sections also serve as a baseline against which future inelastic scattering calculations, carried out in a more comprehensive framework (e.g. in the context of the SciDAC-II project "Building a Universal Nuclear Energy Density Functional" [11, 13]) can be compared.

In the remainder of this introduction the Surrogate formalism and the notion of the spin-parity ($J\pi$) population mismatch are explained, and a brief description of the challenges involved in a comprehensive treatment of the problem is given. In Section 2, a model is introduced for the prediction of the $J\pi$ population

resulting from inelastic alpha scattering off a spherical target. The model employed here is based on a particle-hole description of the excited intermediate nucleus. The application of the model requires determining single-particle orbitals, single-particle damping widths, and the interaction between the projectile and the target. These issues are discussed in Sections 3 (single-particle orbitals), 4 (damping widths), and 5 (α-target interaction), respectively. Cross sections for producing individual particle-hole excitations are shown in Section 6, and the final inelastic scattering cross section and the associated $J\pi$ distributions are given in Section 7 for 140 MeV α particles scattering from a ^{90}Zr target. A summary and recommendations for future work are given in Section 8.

1.1 The Surrogate formalism and the spin-parity population mismatch

The Surrogate nuclear reaction technique combines experiment with theory to obtain cross sections for compound-nuclear reactions, $a + A \rightarrow B^* \rightarrow c + C$, involving difficult-to-produce targets, A. In the Hauser-Feshbach formalism [47], the cross section for this desired reaction takes the form:

$$\sigma_{\alpha\chi}(E_a) = \sum_{J,\pi} \sigma_\alpha^{CN}(E_{ex}, J, \pi)\ G_\chi^{CN}(E_{ex}, J, \pi)\,, \tag{1}$$

with α and χ denoting the relevant entrance and exit channels, $a + A$ and $c + C$, respectively [47]. The excitation energy E_{ex} of the compound nucleus, B^*, is related to the center-of-mass energy E_a in the entrance channel via the energy needed for separating a from B: $E_a = E - S_a(B)$. In many cases the formation cross section $\sigma_\alpha^{CN} = \sigma(a + A \rightarrow B^*)$ can be calculated to a reasonable accuracy by using optical potentials, while the theoretical decay probabilities G_χ^{CN} for the different decay channels χ are often quite uncertain. The latter are difficult to calculate accurately since they require knowledge of optical models, level densities, and strength functions for the various possible exit channels. The objective of the Surrogate method is to determine or constrain these decay probabilities experimentally.
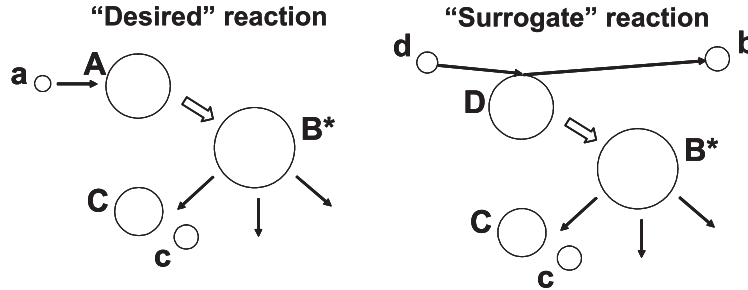
Figure 1: Schematic representation of the desired (left) and Surrogate (right) reaction mechanisms. The basic idea of the Surrogate approach is to replace the first step of the desired reaction, $a+A$, by an alternative (Surrogate) reaction, $d + D \rightarrow b + B^*$, that populates the same compound nucleus. The subsequent decay of the compound nucleus into the relevant channel, $c + C$, can then be measured and used to extract the desired cross section.

In the Surrogate approach, the compound nucleus B^* is produced by means of an alternative (Surrogate), direct reaction, $d + D \rightarrow b + B^*$, and the desired decay channel $\chi(B^* \rightarrow c + C)$ is observed in coincidence with the outgoing particle b (see Figure 1). The coincidence measurement provides

$$P_{\delta\chi}(E_{ex}) = \sum_{J,\pi} F_\delta^{CN}(E_{ex}, J, \pi)\ G_\chi^{CN}(E_{ex}, J, \pi)\,, \tag{2}$$

the probability that the compound nucleus was formed in the Surrogate reaction with spin-parity distribution $F_\delta^{CN}(E_{ex}, J, \pi)$ and subsequently decayed into the channel χ. The distribution $F_\delta^{CN}(E_{ex}, J, \pi)$, which may be very different from the compound-nuclear spin-parity populations following the absorption of the projectile a in the desired reaction, has to be determined theoretically, so that the branching ratios $G_\chi^{CN}(E_{ex}, J, \pi)$ can be extracted from the measurements. In practice, the decay of the compound nucleus is modeled and the

4

$G_\chi^{CN}(E_{ex}, J, \pi)$ are obtained by adjusting parameters in the model to reproduce the measured probabilities $P_{\delta\chi}(E_{ex})$ [78, 79]. Subsequently, the sought-after cross section can be obtained by combining the calculated cross section $\sigma_\alpha^{CN}(E_{ex}, J, \pi)$ for the formation of B^* (from $a + A$) with the extracted decay probabilities $G_\chi^{CN}(E_{ex}, J, \pi)$ for this state, see Eq. 1.

The formalism outlined above does not include correlations between the incident and outgoing reaction channels, which in principle affect both the desired and Surrogate reactions. For the desired reaction, these correlations can be taken into account formally by including width fluctuation corrections [45], while their influence on the coincidence probability determined in a Surrogate experiment, Eq. 2, remains to be quantified.

The single most important challenge associated with the Surrogate approach is the fact that the Surrogate reaction populates the states in the intermediate nucleus differently than the desired channel, i.e. the weights $F_\delta^{CN}(E_{ex}, J, \pi)$ by which the decay probabilities $G_\chi^{CN}(E_{ex}, J, \pi)$ are multiplied in Eq. 2 are different from the relative formation cross sections $f_\alpha^{CN}(E_{ex}, J, \pi) = \sigma_\alpha^{CN}(E_{ex}, J, \pi)/\sum_{J'\pi'} \sigma_\alpha^{CN}(E_{ex}, J', \pi')$ of Eq. 1, and depend on the direct reaction under consideration. This diffference is often referred to as the *spin-parity population mismatch*. Almost all applications of the Surrogate method so far have neglected the effects of the spin-parity mismatch and have analyzed the data under the assumption that the Weisskopf-Ewing approximation is valid [22, 17, 62, 15, 9, 63, 60, 19, 8].

In the *Weisskopf-Ewing approximation* [45, 24] to the full Hauser-Feshbach formalism, the compound-nuclear decay probabilities are treated as independent of J and π, and the cross section for the desired reaction takes the simple product form:

$$\sigma_{\alpha\chi}^{WE}(E_a) = \sigma_\alpha^{CN}(E_{ex}) \; \mathcal{G}_\chi^{CN}(E_{ex}), \tag{3}$$

where $\sigma_\alpha^{CN}(E_{ex}) = \sum_{J,\pi} \sigma_\alpha^{CN}(E_{ex}, J, \pi)$ is the reaction cross section describing the formation of the compound nucleus in the desired reaction and $\mathcal{G}_\chi^{CN}(E_{ex})$ denotes the $J\pi$-independent decay probability for the exit channel χ. In the context of Surrogate reactions, this approximation greatly simplifies the application of the method: It becomes straightforward to obtain the $J\pi$-independent branching ratios $\mathcal{G}_\chi^{CN}(E_{ex})$ from measurements of $P_{\delta\chi}(E_{ex})$ [$= \mathcal{G}_\chi^{CN}(E_{ex})$ since $\sum_{J,\pi} F_\delta^{CN}(E_{ex}, J, \pi) = 1$] and to calculate the desired reaction cross section. Calculating the direct-reaction probabilities $F_\delta^{CN}(E_{ex}, J, \pi)$ and modeling the decay of the compound nucleus are no longer required.

The recently introduced *Surrogate Ratio approach* [63, 60, 19, 8] is an approximation that makes use of the Surrogate idea and requires the (approximate) validity of the Weisskopf-Ewing limit. In this approach, the ratio $R(E) = \sigma_{\alpha_1\chi_1}/\sigma_{\alpha_2\chi_2}$ of the cross sections of two compound-nuclear reactions is measured, using two Surrogate experiments. An independent determination of the cross section $\sigma_{\alpha_1\chi_1}$ can then be used to deduce $\sigma_{\alpha_2\chi_2}$. An advantage of using the Ratio method is the fact that it eliminates the need to accurately measure the total number of Surrogate reaction events. Furthermore, there are indications that small to moderate deviations from the Weisskopf-Ewing assumption might cancel in this approach [38, 36].

Both the Weisskopf-Ewing approximation and the related Surrogate Ratio approach have provided useful cross section information [22, 17, 62, 15, 9, 63, 60, 19, 8], in particular for (n, f) cross sections for actinide nuclei. However, at low incident energies (below about $E_n = 1$ MeV for neutron-induced fission) and for reactions involving targets near closed shells, it is known that the Weisskopf-Ewing approximation is no longer valid [78, 43, 57, 58, 39]. Furthermore, (n, γ) reactions are expected to be more sensitive to the compound-nucleus spin-parity distribution than (n, f) reactions. Thus, a treatment that addresses the spin-parity population mismatch issue is needed in order to investigate the validity of the Weisskopf-Ewing and Ratio approximations, to apply the Surrogate approach to new areas of interest, and to determine its limitations.

1.2   Addressing the challenge of the spin-parity mismatch

Predicting the spin-parity distribution for a compound nucleus produced in a Surrogate reaction requires a careful consideration of the reaction mechanisms that are involved in the formation of the compound nucleus. In the absence of width fluctuation corrections, the challenge of describing the relevant reaction mechanisms can be divided into two separate problems:

  1) the formation of a highly-excited nucleus in a direct reaction, and

2) the damping of the excited states into the compound nucleus.

The above considerations do not include correlations between the incident and outgoing reaction channels, which in principle affect both the desired and Surrogate reactions. For the desired reaction, these correlations can be taken into account formally by including width fluctuation corrections [45], while a similar simple solution is not readily available for the Hauser-Feshbach-type expression describing the Surrogate reaction, Eq. 2. Therefore, a comprehensive theoretical treatment of the Surrogate method requires an assessment of the importance of

3) width fluctuation correlations to the Surrogate reaction formalism and possibly an extension of the formalism to account for these correlations.

Addressing the first problem necessitates developing a quantitative description of the direct-reaction process that allows for a prediction of the spin-parity distribution in the highly-excited intermediate nucleus, immediately following the direct reaction. Such a description is also nontrivial since it requires a framework for calculating cross sections of different reactions (stripping, pick-up, charge exchange, and inelastic scattering) to continuum states, for a variety of projectiles (p, d, t, α, etc.) and targets (spherical, deformed, and transitional).

The second problem is associated with the subsequent evolution of the intermediate nucleus. The assumption that a compound (i.e. equilibrated) nucleus is formed is central to the Surrogate method. Rapid decay of the intermediate configuration before a compound nucleus can be formed would invalidate the Surrogate analysis. The competition between particle emission and equilibration, and its dependence on the spin and parity of the intermediate nucleus, needs to be investigated[1].

Incorporating width fluctuation correlations will introduce additional complications. In the desired reaction, they are known to enhance the elastic scattering cross section and reduce the inelastic and reaction cross sections, although this depletion rarely exceeds 10-20% (even at energies below approximately 2 MeV) and becomes negligible as the excitation energy of the compound nucleus increases [45]. An examination of the role of width fluctuation correlations for Surrogate reactions is beyond the scope of the present work, but should be part of a comprehensive investigation of the formalism associated with the Surrogate approach.

---

[1]This process should not be confused with pre-equilibrium emission of particles in the desired reaction, $a + A \rightarrow c + C$; contributions from the latter cannot be determined via the Surrogate approach and need to be calculated separately and added to the desired cross section.

2   The Model

The goal of the work presented here is the prediction of the angular-momentum and parity distribution in a compound nucleus following a direct inelastic-scattering reaction with α particles from a spherical or near-spherical target nucleus. A complete description of the process in which the compound nucleus is produced is nontrivial, since it involves ingredients that have not been sufficiently explored to date (see Section 1.2). To make a calculation of the $J\pi$ distribution in the compound nucleus of interest feasible, we employ a series of assumptions and simplifications. These will be described below. The result is a simple model that allows a first prediction of the angular-momentum distribution in a spherical compound nucleus that was excited by inelastic alpha scattering. Ideas for improving the model will be discussed in Section 8.

2.1   Producing a compound nucleus via inelastic scattering: Qualitative description

We consider one-step inelastic scattering in which a projectile b excites the target B from its ground state to an intermediate state B^* and restrict ourselves to nuclear interactions that are of two-body nature. This process has been studied in much detail for bound final states, in particular for collective excitations. More generally, it is possible to excite a collective mode or 1p-1h states, where the notation p (h) refers to a single-nucleon, proton or neutron, particle (hole) state.

   We now consider the case in which inelastic scattering produces a highly excited 1p-1h excitation $|\Psi_{1p1h}\rangle$ in the A-body system. E_{ex} is the energy that was transferred in the scattering process. If E_{ex} is larger than the particle separation energy, then the nucleus can emit a particle or produce a 2p-2h state $|\Psi_{2p2h}\rangle$. Subsequently, the system can evolve to 3p-3h, 4p-4h, etc. states. At each step it is possible that the system emits a particle, although the probability for particle emission decreases with each further step since the energy E_{ex} is shared among more and more nucleons. If no particle is emitted in this chain, the process produces a compound A-body system. Similar considerations apply to any excited configuration that can be described as a superposition of 1p-1h states.

   In principle, one would like to describe the evolution of the intermediate nucleus following the initial excitation by inelastic scattering. Such a description is beyond the scope of the current study. In the remainder of the document we will restrict our efforts to predicting the $J\pi$ distribution of an intermediate nucleus immediately following the (Surrogate) direct inelastic scattering process. The result can be used as a first estimate for the spin-parity distribution present in the compound nucleus prior to decay. This is equivalent to assuming that, to first order, the $J\pi$ distribution is not affected by the equilibration process. This assumption is likely to be violated and the uncertainty introduced by this simplification remains to be studied.

   Next, we will consider the excitation of a nucleus B from its ground state to an excited state B^* with fixed energy E_{ex} via inelastic scattering. We are interested in energy regions with high level density and will consider excitations energies E_{ex} both lower and higher than the neutron and proton separation energies of the nucleus. We will carry out calculations for a fixed excitation energy; it is straightforward to generalize from this case to a situation in which a finite energy interval is populated, as is the case in a Surrogate reaction.

2.2   DWBA description for inelastic alpha scattering

We describe the scattering process as a one-step process and employ the DWBA formalism [67, 46]. The scattering cross section is proportional to the square of the matrix element

$$M = \int d\vec{r}_\alpha \, d\vec{r} \, \chi^{-*}(k_f, \vec{r}_\alpha) \Psi_f^{(A)*}(\vec{r}) V(\vec{r}_0, \vec{r}) \Psi_i^{(A)}(\vec{r}) \chi^+(k_i, \vec{r}_\alpha) \, , \tag{4}$$

where $\Psi_k^{(A)}(\vec{r}) = \Psi_k^{(A)}(\vec{r}_1, \ldots, \vec{r}_A)$ denotes the A-body wave function for the initial ($k = i$) and final ($k = f$) states of the target, and $\chi^+(k_i, \vec{r}_\alpha)$ and $\chi^{-*}(k_f, \vec{r}_\alpha)$ are the distorted waves in the entrance and exit channels, respectively. We have used the notation $\vec{r} = (\vec{r}_1, \ldots, \vec{r}_A)$ and $\vec{r}_0$ for the laboratory coordinates of the target nucleons and the projectile, respectively. The channel coordinate is $\vec{r}_\alpha = \vec{r}_0 - \frac{1}{A} \sum_{i=1,\ldots,A} \vec{r}_i$. We

introduce internal coordinates which are defined with respect to the center of mass of the target nucleus, $\vec{\xi}_j = \vec{r}_j - \frac{1}{A}\sum_{i=1,...,A}\vec{r}_i$, and assume the interaction between projectile and target to be of two-body type:

$$V(\vec{r}_0,\vec{r}) \quad = \quad \sum_{j=1,...,A} V(|\vec{r}_0 - \vec{r}_j|) = \sum_{j=1,...,A} V(|\vec{r}_\alpha - \vec{\xi}_j|) . \tag{5}$$

The matrix element of Eq. 4 then takes the form:

$$M \quad = \quad \sum_{j=1,...,A} \int d\vec{r}_\alpha \, d\vec{\xi}_1 \ldots d\vec{\xi}_A \, \chi^{-*}(k_f,\vec{r}_\alpha)\Psi_f^{(A)*}(\vec{\xi}_1,\ldots,\vec{\xi}_A)$$

$$\times \quad V(|\vec{r}_\alpha - \vec{\xi}_j|)\Psi_i^{(A)}(\vec{\xi}_1,\ldots,\vec{\xi}_A)\chi^+(k_i,\vec{r}_\alpha) , \tag{6}$$

We note that any A-body wave function can be written in the following form [35]:

$$\Psi_k^{(A)}(\vec{\xi}_1,\ldots,\vec{\xi}_A) \quad = \quad \frac{1}{\sqrt{A}}\sum_n \mathcal{A}[\phi_n^k(\vec{\xi}_1)\Psi_n^{(A-1)}(\vec{\xi}_2,\ldots,\vec{\xi}_A)] . \tag{7}$$

Here $\Psi_k^{(A)}$ ($\Psi_n^{(A-1)}$) denotes the fully anti-symmetric wave function of the k-th (n-th) excited state of the A-body ($(A-1)$-body) system, $\phi_n^k(\vec{\xi}_1)$ is the associated one-body overlap function, and $\mathcal{A}$ is an ("inter-cluster") antisymmetrization operator that ensures proper behavior with respect to exchange between the labels $\vec{\xi}_1$ and $\vec{\xi}_j$ ($j = 2,\ldots,A$). Note that this expansion is exact if the sum includes all states of the $(A-1)$-body system, including continuum states.

Using the orthonormality of the $(A-2)$-body functions $\Psi_n^{(A-1)}$ and $\Psi_m^{(A-1)}$, we obtain

$$M \quad = \quad \sum_{j=1,...,A} \frac{1}{A}\sum_m \int d\vec{r}_\alpha \, d\xi_j \, \chi^{-*}(k_f\vec{r}_\alpha)\phi_m^{f*}(\vec{\xi}_j)V(|\vec{r}_\alpha - \vec{\xi}_j|)\phi_m^i(\vec{\xi}_j)\chi^+(k_i\vec{r}_\alpha)$$

$$= \quad \sum_m \int d\vec{r}_\alpha \, d\xi_1 \, \chi^{-*}(k_f\vec{r}_\alpha)\phi_m^{f*}(\vec{\xi}_1)V(|\vec{r}_\alpha - \vec{\xi}_1|)\phi_m^i(\vec{\xi}_1)\chi^+(k_i\vec{r}_\alpha) , \tag{8}$$

with the sum running over all states $\Psi_m^{(A-1)}$ of the $(A-1)$-body system. In the derivation of this expression, we have neglected the effects of the antisymmetrization operator and used the fact that the terms for each value of j are identical. The importance of corrections due to the antisymmetrization present in Equation 7 remains to be studied. Recoil effects, as well as exchange between target and projectile nucleons, have also been neglected in the above discussion. The former issue will be addressed below, while the latter will be assumed negligible, since the focus here is on inelastic alpha scattering and we treat the alpha particle as inert.

In general, the overlap functions ϕ_n^k are very complicated since they contain information on the structure of both the A and $(A-1)$-body systems. In many practical applications, however, they are approximated by single-particle wave functions φ_n^k that are solutions to the one-body Schrödinger equation with a local potential. Positive-energy solutions, corresponding to scattering states, are normalized asymptotically, while the norm of a negative-energy solution is given by the associated spectroscopic factor, $S_n^k = \int dr |\varphi_n^k(r)|^2$, with $S_n^k \leq 1$.

It is instructive to consider Equation 8 in the strict independent-particle model. In this limit, the overlap functions reduce to single-particle functions with norm one and each term in the sum $(\sum_m \ldots)$ corresponds to a nucleon making a transition from an inital orbital φ_m^i to a final orbital φ_m^f (see Figure 2). The energy associated with this transition is $E_{ex} = E_{m_h} + E_{m_p}$, where E_{m_p} and E_{m_h} are the binding energies of the hole and particle orbitals, respectively. A more realistic nuclear-structure model includes nuclear interactions beyond the mean field of the independent-particle model.

2.3 Inelastic scattering to a region of high level density

We are interested in describing an inelastic-scattering process that excites a nucleus from an inital state $\Psi_i^{(A)}$ to a final, highly-excited state $\Psi_f^{(A)}$ at energy E_{ex}. In general, we do not have a reliable description of the
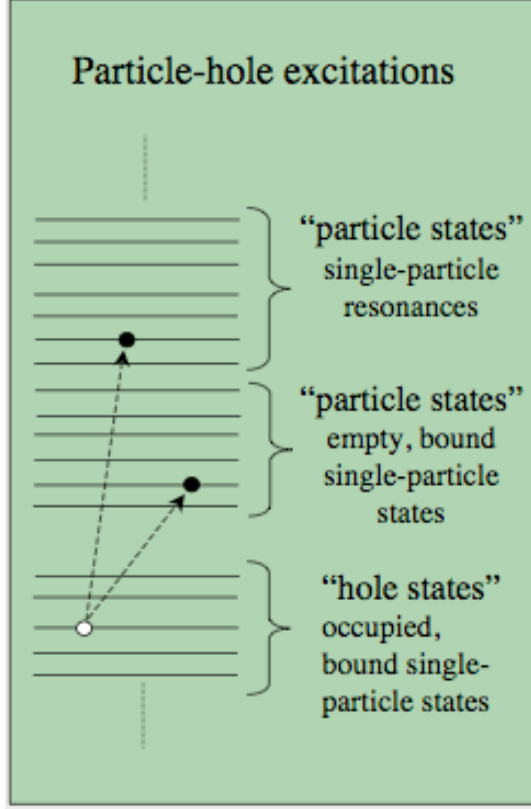
Figure 2: Particle-hole excitations included in the model of the inelastic scattering process. A nucleon makes the transition from an occupied, bound single-particle state (open circle) to an empty single-particle state (filled circle). Transitions to bound as well as unbound (resonance) states have to be considered.

structure of $\Psi_f^{(A)}$. However, we are interested in a region of high level density and need to be concerned only with average properties of the cross section. This allows us to introduce some simplifications. If we assume that one-step inelastic scattering will create some linear combination of particle-hole excitations in the target nucleus, we can write the relevant matrix element in the form:

$$M_{ph} = \sum_{m_h, m_p} a(m_h, m_p) \int d\vec{r}_\alpha \, d\xi_1 \, \chi^{-*}(k_f \vec{r}_\alpha) \varphi^*_{m_p}(\vec{\xi}_1) V(|\vec{r}_\alpha - \vec{\xi}_1|) \varphi_{m_h}(\vec{\xi}_1) \chi^+(k_i \vec{r}_\alpha) \,, \qquad (9)$$

where φ_{m_h} (φ_{m_p}) is a single-particle orbital that is occupied (empty) in the initial target nucleus and empty (occupied) in the final state. The sum $\sum_{m_h, m_p} \ldots$ includes all particle-hole combinations that are consistent with the relevant conservation rules (energy, angular momentum, parity). Each weight factor $a(m_h, m_p)$ provides a measure of the strength with which a particular (m_h, m_p) combination is represented in the state $\Psi_f^{(A)}$, i.e.

$$a(m_h, m_p) \equiv \langle \Psi_f^{(A)} | \Phi_{m_h, m_p}^{(A)} \rangle \,, \qquad (10)$$

where $\Phi_{m_h, m_p}^{(A)}$ denotes the A-body configuration that is obtained when a nucleon is removed from an occupied single-particle orbital φ_{m_h} of the reference state and placed into an empty orbital φ_{m_p}. The reference state relevant for our purposes is the ground state of the target nucleus, $\Psi_i^{(A)}$. Obviously, the weight factors contain information on the structure of both the initial and the final target states. Here we will introduce a simple model for these factors.

In the strict independent-particle model (IPM), the configuration $\Phi^{(A)}_{m_h, m_p}$ has a sharp energy, $E_{(m_h, m_p)} = E_{m_h} + E_{m_p}$, where E_{m_p} and E_{m_h} are the binding energies of the hole and particle orbitals, respectively. In a more realistic description, this particle-hole configuration is spread over many A-body states, $i.e.$ the weight factor of Equation 10 is a function of energy, $a(m_h, m_p) = f(E - E_{(m_h, m_p)})$, with $\int_\infty^\infty dE\, f(E - E_{(m_h, m_p)}) = 1$. We take the distribution to be of Lorentzian shape, centered at $E = E_{(m_h, m_p)}$:

$$f(E - E_{(m_h, m_p)}) \quad = \quad \frac{1}{2\pi} \frac{\Gamma_{m_h, m_p}}{(E - E_{(m_h, m_p)})^2 + (\Gamma_{m_h, m_p}/2)^2} \ , \tag{11}$$

where Γ_{m_h, m_p} is the damping (or spreading) width of the particle-hole configuration. Single-particle energies and wave functions are obtained in Section 3 and the appropriate values for the damping widths are determined in Section 4.

Contributions from different particle-hole excitations interfere since the inelastic scattering cross section is proportional to the square of the matrix element M_{ph}. In a further simplification, we assume that we can neglect the cross terms, $i.e.$ we approximate the inelastic cross section by the incoherent sum

$$\frac{d\sigma}{d\Omega} \quad \approx \quad \sum_{m_h, m_p} |a(m_h, m_p)|^2 \left(\frac{d\sigma}{d\Omega}\right)_{m_h, m_p} . \tag{12}$$

Here $\left(\frac{d\sigma}{d\Omega}\right)_{m_h, m_p}$ denotes the cross section for creating the particle-hole excitation (m_h, m_p) at energy $E_{(m_h, m_p)}$; it is proportional to the square of

$$\mu^f_{m_h, m_p} \quad = \quad \int d\vec{r}_\alpha\, d\xi_1\, \chi^{-*}(k_f \vec{r}_\alpha) \varphi^*_{m_p}(\vec{\xi}_1) V(|\vec{r}_\alpha - \vec{\xi}_1|) \varphi_{m_h}(\vec{\xi}_1) \chi^+(k_i \vec{r}_\alpha) . \tag{13}$$

Cross sections for inelastic scattering to specific particle-hole excited configurations are presented in Section 6. The incoherent-sum approximation is then used to calculate the total cross section for producing ^{90}Zr at 10 MeV excitation energy via inelastic scattering with 140 MeV alpha particles. The results are discussed in Section 7.

2.4 Recoil effects

In Equation 8, we have neglected recoil effects. To avoid introducing spurious excitations of the A-body target nucleus into our model, we employ internal coordinates, which are defined with respect to the center of mass of the target. As a result, target excitations are induced by the interaction of the projectile with an individual nucleon (which moves the nucleon relative to the center of mass of the target), as well as by the interaction of the projectile with the remainder of the target, the 'core' (which moves this remainder relative to the center of the mass of the target). Both contribute to a given particle-hole excitation. To account for this, we replace $\mu^f_{m_h, m_p}$ in Equation 13 by

$$\mu_{m_h, m_p} \quad = \quad \mu^f_{m_h, m_p} + \mu^c_{m_h, m_p} \ , \tag{14}$$

where

$$\mu^c_{m_h, m_p} \quad = \quad \int d\vec{r}_\alpha\, d\xi_1\, \chi^{-*}(k_f \vec{r}_\alpha) \varphi^*_{m_p}(\vec{\xi}_1) U_F(|\vec{r}_\alpha + \frac{1}{A-1} \vec{\xi}_1|) \varphi_{m_h}(\vec{\xi}_1) \chi^+(k_i \vec{r}_\alpha) . \tag{15}$$

Here $\vec{r}_\alpha + \frac{1}{A-1} \vec{\xi}_1$ is a vector that points from the projectile to the center of mass of the $(A-1)$-body 'core' and U_F is an optical potential that is obtained by folding the two-body interaction with the density of the core. The potential is taken to be independent of the excitation energy of the $(A-1)$-body core. We will approximate it by a phenomenological optical potential that describes the interaction of the projectile with the relevant $(A-1)$-body nuclear system (^{89}Zr or ^{89}Y here).

Note that the formalism described here does not assume that the target nucleus has a core-plus-valence structure with an inert core containing orbitals which do not participate in the nuclear excitation. Instead, nucleons from each occupied orbital can be excited by inelastic scattering (subject to energy conservation). This is reflected in the sum over all occupied states m_h in Equation 12. Each 'hole' term corresponds to

a particular 'core' configuration and contributions from the projectile interacting with both the nucleon involved in the particle-hole transition and with the remaining core need to be included in the cross section calculation.

Details of the formalism summarized here are discussed elsewhere [28]. For the application discussed in this report, we employed the direct-reaction code FRESCO [75] to calculate the individual cross sections $\left(\frac{d\sigma}{d\Omega}\right)_{m_h,m_p}$. The optical model potentials for the projectile-target and projectile-core interactions are discussed in Sections 5.1-5.2 and the form of the projectile-nucleon interaction $V(|\vec{r}_\alpha - \vec{\xi}_1|)$ is discussed in Sections 5.3-5.4.

3 Single-nucleon Orbitals for Particle and Hole States

To obtain DWBA cross sections for inelastic scattering we need to calculate the matrix element given in Equation 14 for all possible particle-hole combinations (m_p, m_h) in the energy range of interest. Here, we are interested in obtaining $J\pi$ distributions for ^{90}Zr excited to $E_{ex} \approx 10$ MeV, $i.e.$ we need to consider 1p-1h excitations that have energies lying in an interval of several MeV below E_{ex} to several MeV above E_{ex}. In particular, we need to determine wave functions for the single-particle orbitals φ_{m_p} and φ_{m_h}. We obtain the bound (occupied as well as empty) orbitals by solving the one-body Schrödinger equation with a local potential. We use the real part of the global optical model by Koning and Delaroche [54], which includes volume, surface, and spin-orbit terms, and adjust the strength of the volume term in order to reproduce experimental binding energies and subsequently calculate the associated wave functions. Fortunately, the structure of ^{90}Zr, the nucleus of interest here, has been extensively studied. Experimental information on the single-particle binding energies E_B in ^{90}Zr is available from pickup, stripping, and knock-out experiments. The literature values used for our study are summarized in the next section. Throughout this report, we list the binding energies as positive values for bound states and negative values for resonance states. We also determine, separately for neutrons and protons, average potentials that yield overall good fits to the relevant binding energies. These average potentials are used to determine the wave functions of the unbound orbitals. For our applications, we are primarily interested in those unbound states that do not decay by particle emission ($i.e.$ correspond to breakup of the target), but lead to np-nh excitations. These are best approximated by single-particle resonances. In Section 3.2 we determine the neutron and protons resonance energies by calculating the relevant phase shifts. The associated wave functions can be described approximately in the weak-binding approximation or by employing bin functions. Wave functions and cross sections obtained from these methods are compared to each other in Sections 3.3 and 3.4, respectively.

3.1 Single-particle binding energies and the binding potential

Information on single-particle binding energies can be obtained from one-nucleon pickup and stripping reactions. Table 1 lists the energies for occupied and empty neutron states in the nucleus ^{90}Zr . We refer to the occupied states as "hole" state (states 1–5) and the empty states as "particle" states (states 6–10). They correspond to hole states in ^{89}Zr and particle states in ^{91}Zr , respectively. Energies for the former are obtained from ^{90}Zr(p,d)^{89}Zr measurements, see Table IV of Ref. [27], and energies for the latter result from one-neutron transfers with Ne isotopes, see Table I of Ref. [44]. The Fermi energy is taken to be the energy that lies halfway between the last occupied and the first unoccupied neutron orbital, i.e. E_F(n,^{90}Zr)=9.78 MeV.

Table 1: Literature values for binding energies of single-particle neutron orbitals, E_B. States 1-5 are occupied ("hole") orbitals, and states 6-10 are bound unoccupied ("particle") orbitals. The symbol E_{ex} refers to the exciation energy in the relevant final nucleus, ^{89}Zr or ^{91}Zr. It is related to the binding energy E_B via the neutron separation energy in ^{90}Zr: $E_B = E_{ex} + S_n$, where $S_n(^{90}$Zr$) = 11.970$ MeV and $S_n(^{91}$Zr$) = 7.1945$ MeV.

No.	orbital	n	l	j	"E_{ex}" [MeV]	E_B [MeV]
1	$1f_{7/2}$	1	3	3.5	9.02	20.99
2	$1f_{5/2}$	1	3	2.5	2.91	14.88
3	$2p_{3/2}$	2	1	1.5	2.14	14.11
4	$2p_{1/2}$	2	1	0.5	1.11	13.08
5	$1g_{9/2}$	1	4	4.5	0.40	12.37
6	$2d_{5/2}$	2	2	2.5	0.00	7.195
7	$3s_{1/2}$	3	0	0.5	1.20	5.990
8	$1g_{7/2}$	1	4	3.5	2.19	4.995
9	$2d_{3/2}$	2	2	1.5	2.03	5.153
10	$1h_{11/2}$	1	5	5.5	4.05	3.145

Table 2 lists binding energies for proton single-particle states. The data are taken from Y. Wang *et al.* [76], Table III, which compiles information from other references. The results for the hole orbitals (states 1-7) are based on the $(e, e'p)$ data from den Herder *et al.* [23] and the energies for the particle orbitals (states 8-10) are based on (^{3}He,d) data from Finkel *et al.* [40]. The Fermi energy for protons in ^{90}Zr is found to be $E_F(\text{p},^{90}\text{Zr})$=6.75MeV, which is in agreement with the valued 6.8 MeV, determined by Wang *et al.* [76].

Table 2: Literature values for binding energies of single-particle proton orbitals. States 1-7 are occupied ("hole") orbitals, and states 8-10 are bound unoccupied ("particle") orbitals, E_B. The symbol E_{ex} refers to the exciation energy in the relevant final nucleus, ^{89}Y or ^{91}Nb . The proton separation energies for ^{90}Zr and ^{91}Nb are $S_p(^{90}\text{Zr}) = 8.3548$ MeV and $S_p(^{91}\text{Nb}) = 5.1588$ MeV. Note: In Ref. [76], the energy value of 23.8 MeV is an average for the $1d_{5/2}$ and $1d_{3/2}$ orbits. Here, we assign both the same energy.

No.	orbital	n	l	j	"E_{ex}" [MeV]	E_B [MeV]
1	$1d_{5/2}$	1	2	2.5	15.45	23.80
2	$1d_{3/2}$	1	2	1.5	15.45	23.80
3	$2s_{1/2}$	2	0	0.5	13.45	21.80
4	$1f_{7/2}$	1	3	3.5	8.646	17.00
5	$1f_{5/2}$	1	3	2.5	2.446	10.80
6	$2p_{3/2}$	2	1	1.5	2.046	10.40
7	$2p_{1/2}$	2	1	0.5	0.00	8.3545
8	$1g_{9/2}$	1	4	4.5	0.004	5.11
9	$2d_{5/2}$	2	2	2.5	3.85	1.30
10	$1g_{7/2}$	1	4	3.5	4.81	0.34

The binding energies from the tables above were used to obtain average binding potentials for neutrons and protons in ^{90}Zr, respectively. The real part of the global optical potential from Koning and Delaroche was used to fix all parameters, except for the strength of the Wood-Saxon volume term, which was adjusted to obtain an overall good fit to the single-nucleon binding energies above. The resulting potential has the form:

$$V_{bind}(r) = V_C(r) - V_0 \frac{1}{1 - \exp\left(\frac{r - R_0}{a_0}\right)} - V_{ls} \frac{\hbar^2}{2m_\pi^2 c^2} \frac{\exp\left[-\left(\frac{r - R_{ls}}{a_{ls}}\right)\right]}{a_{ls} r \left(1 + \exp\left[-\left(\frac{r - R_{ls}}{a_{ls}}\right)\right]\right)^2} \vec{l} \cdot \vec{s} \qquad (16)$$

where $\hbar^2/(2m_\pi^2 c^2) \approx 2$, $R_x = r_x A_{target}^{1/3}$ for $x = 0, ls, C$, and $V_C(r)$ is the Coulomb potential. The parameters for the average neutron and proton binding potentials are listed in Table 3. In subsequent calculations that involve resonance (unbound particle) states, these parameters are held fixed. In calculations that determine wave function of the bound states, the strengths V_0 are adjusted to reproduce the binding energies above.

Table 3: Parameters for the neutron and proton binding potentials. Note that the radii r_0, r_{ls}, and r_C have to be scaled by $A_{target}^{1/3}$.

Parameter	Neutrons	Protons
V_0 [MeV]	53.2320	61.0030
r_0 [fm]	1.2130	1.2130
a [fm]	0.664	0.664
V_{ls} [MeV]	6.1500	5.9800
r_{ls} [fm]	1.0410	1.0410
a_{ls} [fm]	0.5900	0.5900
r_{0C} [fm]	n/a	1.2400

3.2 Resonance energies via phase shifts

Solving the radial Schrödinger equation with the above potentials for positive energies allows us to determine the single-particle resonance energies and wave functions. We have employed two different methods for determining the resonance energies: a) the method of analytic continuation of the coupling constant (ACCC method), and b) the calculation of phase shifts as a function of energy. The ACCC method is based on the assumption that resonances can be thought of as the continuation of bound states when the strength of the binding potential decreases. In recent years, the ACCC method has been explored and applied for both spherical and deformed systems [73, 74, 20]. Energies, widths, and wave functions for resonances have been calculated in the ACCC approach and compared to exact calculations. The ACCC results were found to provide useful approximations to the quantities obtained with the more complex and time-consuming exact methods. In the current context the method was employed to obtain a first estimate of the possible single-particle resonance energies for both protons and neutrons. The results were then employed to ensure that the determination of resonance energies from a phase shift analysis did not miss narrow resonances.

More specifically, the neutron and proton potentials given in Equation 16 and Table 3 were used to determine the binding energies for single-particle states $\varphi_{nlj}(r)$ that were expected to correspond to resonances. The depth V_0 was increased so that the orbitals $\varphi_{nlj}(r)$ were bound by the potential. Subsequently, the strength of the potential was stepwise decreased and the binding energies of the orbitals were determined as a function of the parameter V_0. The resulting functions $E_B(V_0)$ were then extrapolated to the point where the parameter V_0 coincided with the value listed in Table 3 and the extrapolated energy was taken to be the estimated resonance energy, E_{nlj}^{ACCC} for the orbital of interest. While this method does not guarantee the existence of a resonance at energy E_{nlj}^{ACCC}, it allows for a more efficient search of the resonance energy when the phase shift analysis is employed.

Subsequently, the one-body radial Schrödinger equation was solved for positive energies and the phase shifts of the single-particle scattering functions were determined as a function of energy. Resonance energies E_{lj}^{res} were determined by the requirement that the phase shift has to rise through 90 degrees at E_{lj}^{res}. The phase shifts for various neutron and proton scattering states are plotted in Figure 3 and in Figure 4, respectively, and the resulting resonance energies are listed in Tables 4 and 5. Since the phase shift rises rapidly near a resonance, cubic spline fits were used to improve the determination of the resonance energy. The resonance states are completely characterized by their energy, E_{lj}^{res}, and (l, j) quantum numbers. For convenience, we also assign a label n as follows: For fixed depth, V_0, the binding potential, V_{bind} has bound states labeled by (n, l, j), where $n = 1, 2, 3, \ldots$ is the number of nodes in the single-particle bound-state wave function (n includes the node at the origin, but not at inifinity, so $n > 0$). For each pair (l, j) there exists a number $n_{max(l,j)}$ that gives the number of nodes in the weakest-bound single-particle state. With increasing energy, we then label the resonance states $\varphi_{lj}^{res}(r)$ with an additional quantum number $n = n_{max(l,j)} + 1$, $n_{max(l,j)} + 2, \ldots$. While resonance states have an infinite number of nodes, the quantum label n so associated with a resonance can be related to the number of nodes in the single-particle bound-state orbital that will later on be used to approximate the resonance function under consideration.
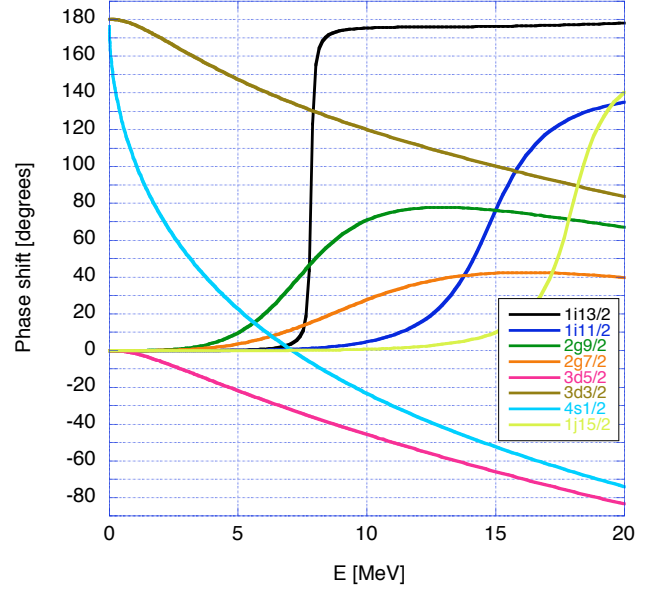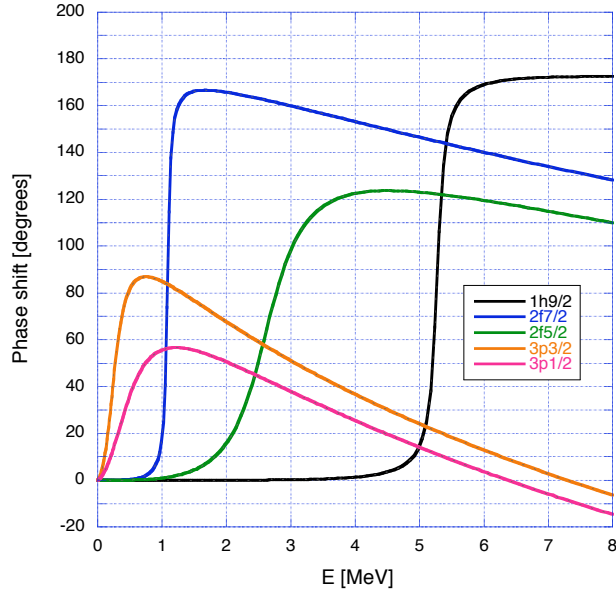
Figure 3: Calculated phase shifts for neutron scattering states associated with the potential given in Equation 16 and Table 3. The legend shows the quantum labels (n, l, j), where (l, j) give the orbital and total angular momentum values of the single-particle resonance and the label n has been assigned as described in the text.
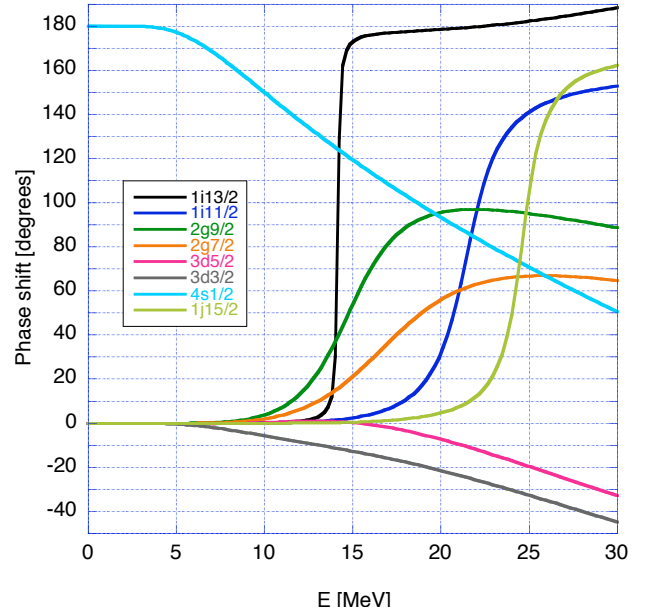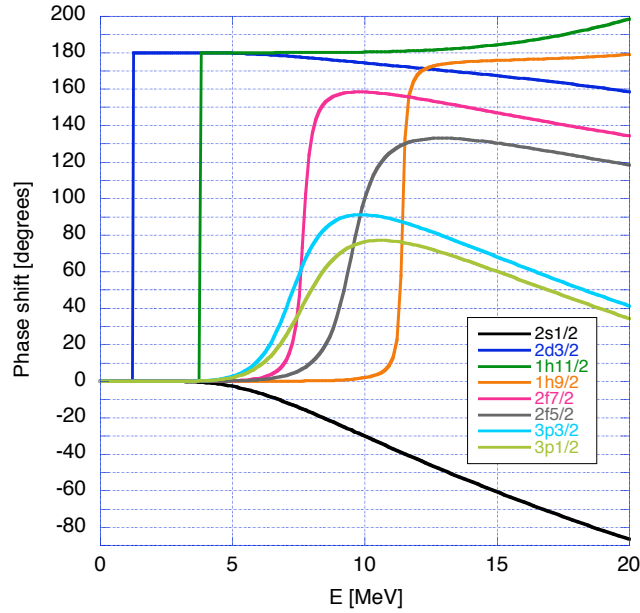

Figure 4: Calculated phase shifts for proton scattering states associated with the potential given in Equation 16 and Table 3. The labels are defined in analogy to those of Figure 3.

Table 4: Energies for neutron resonances in ^{90}Zr from phase shift calculations. "No." labels the single-particle neutron state for the potential under consideration; it is a continuation of the labels in Table 1. E_{lj}^{res} is the resonance energy, as determined from the calculated phase shifts shown in Figure 3. The column labeled "comments" lists the calculated phase shift at the resonance energy. Since the phase shift rises rapidly near the resonance energy and since the (finite) energy step size determines the precision in the phase shift calculation, the exact resonance energy is difficult to determine; the "comments" column lists the phase shift at E_{lj}^{res}. The quantum labels (l, j) give the orbital and total angular momentum values of the single-particle resonance and the label n has been assigned as described in the text.

No.	orbital	n	l	j	E_{lj}^{res} [MeV]	Comments
11	$1h_{9/2}$	1	5	4.5	5.28	δ_l=89.24
12	$2f_{7/2}$	2	3	3.5	1.09	δ_l=91.75
13	$2f_{5/2}$	2	3	2.5	2.89	δ_l=89.81
14	$3p_{3/2}$	3	1	1.5	0.75	δ_l=86.90
15	$3p_{1/2}$	3	1	0.5	(1.21)	no resonance
16	$1i_{13/2}$	1	6	6.5	7.85	δ_l=92.67
17	$1i_{11/2}$	1	6	5.5	15.48	δ_l=89.96
18	$1g_{9/2}$	1	4	4.5	(12.91)	no resonance
19	$1g_{7/2}$	1	4	3.5	(16.15)	no resonance
20	$3d_{5/2}$	3	2	2.5	n/a	no resonance
21	$3d_{3/2}$	3	2	1.5	n/a	no resonance
22	$4s_{1/2}$	4	0	0.5	n/a	no resonance
23	$1j_{15/2}$	1	7	7.5	18.20	δ_l=89.97

Table 5: Energies for proton resonances in ^{90}Zr from phase shift calculations. The labels are defined in analogy to those of Table 4. The ACCC method was very useful for determining the location of the proton $2d_{3/2}$ state at $E_{2,3/2}^{res} = 1.22$ MeV, since the resonance is extremely narrow ($\approx$0.2 eV). The resonance was estimated to be at $E_{2,3/2}^{res,ACCC} = 1.07$ MeV.

No.	orbital	n	l	j	E_{lj}^{res} [MeV]	Comments
11	$3s_{1/2}$	3	0	0.5	n/a	no resonance
12	$2d_{3/2}$	2	2	1.5	1.22	90.0
13	$1h_{11/2}$	1	5	5.5	3.78	δ_l=90.00
14	$1h_{9/2}$	1	5	4.5	11.43	δ_l=90.0
15	$2f_{7/2}$	2	3	3.5	7.18	δ_l=90.00
16	$2f_{5/2}$	2	3	2.5	9.81	δ_l=80.00
17	$3p_{3/2}$	3	1	1.5	9.24	δ_l=90.00
18	$3p_{1/2}$	3	1	0.5	(10.62)	no resonance
19	$1i_{13/2}$	1	6	6.5	14.14	δ_l=89.95
20	$1i_{11/2}$	1	6	5.5	21.83	δ_l=90.0
21	$2g_{9/2}$	2	4	4.5	18.23	δ_l=90.00
22	$2g_{7/2}$	2	4	3.5	(25.93)	δ_l=66.87 (no resonance)
23	$3d_{5/2}$	3	2	2.5	n/a	no resonance
24	$3d_{3/2}$	3	2	1.5	n/a	no resonance
25	$4s_{1/2}$	4	0	0.5	n/a	no resonance
26	$1j_{15/2}$	1	7	7.5	24.73	δ_l=90.00

3.3 Weak binding versus bin description: Radial shape of the single-particle wave function

While it is straightforward to calculate single-particle wave functions $\varphi_{nlj}(r)$ for bound states, there are various possibilities for dealing with reactions that involve continuum (positive-energy) states. It is not immediately obvious how to handle the continuum, since it includes both a structureless (nonresonant) continuum, *i.e.* states that correspond to the breakup of a nuclear system, and resonance states. For our purposes it is appropriate to consider single-particle resonance states.

Many reaction theory applications employ weakly-bound orbitals to approximate resonance functions. Alternatively, it is possible to define "continuum bin states" $\Phi(r)$ as energy averages of positive-energy eigenstates of the potential under consideration [66, 3, 75]:

$$\Phi(r) = \sqrt{\frac{2}{\pi N}} \int_{k_1}^{k_2} w(k)\varphi_k(r) dk \, . \tag{17}$$

Here $\varphi_k(r)$ is a positive-energy ($E_k = \hbar^2 k^2/(2\mu)$) solution of the radial Schrödinger equation with the potential $V_{bind}(r)$, $w(k)$ is some weight function, the form of which is chosen according to the problem under consideration [75], and $N = \int_{k_1}^{k_2} |w(k)|^2 dk$. The bin states are normalized to unity and can be constructed to be orthogonal to all bound states and to other bin states (for energy-independent potentials). They play a prominent role in applications of the CDCC (Continuum-discretized coupled-channels) approach [66], which incorporates the effects of the continuum in descriptions of transfer and breakup reactions. In order to describe narrow resonances, we select $w_1(k) = exp(-i\delta_k)T_k^*$, where δ_k is the scattering phase shift for $\varphi_k(r)$ and T_k is the T-matrix element for $\varphi_k(r)$. An alternative definition of the weight factor, $w_2(k) = exp(-i\delta_k)$, results in bin functions that are more appropriate for the description of breakup states. Below we compare wave functions calculated with both prescriptions to each other and to weakly-bound wave functions. We also vary the width of the energy bin, $E_{k_2} - E_{k_1}$.

Figure 5 (top panel) shows single-particle wave functions obtained in the weak binding approximation for binding energies $E_B = 4.0$ MeV, 2.0 MeV, ..., 0.05 MeV, compared to bin functions, calculated with the weight factor $w_1(k)$ and energy width $E_{k_2} - E_{k_1} = 4.0$ MeV. Both a $1h_{9/2}$ (left side) and a $2f_{7/2}$ (right side) resonance are considered. In both cases, we find that the radial shapes of the wave functions obtained in the weak-binding approximation exhibit little dependence on the selected binding energy. At radii smaller than the range of the nuclear potential, the weak-binding solutions are similar to the bin functions. For larger radii, they decay exponentially, while the bin functions show slowly-damped oscillations, as expected.

Figure 5 (bottom panel) illustrates the effect of different prescriptions for calculating the bin functions. Bin wave functions, calculated with two different weight factors $w_1(k)$ and $w_2(k)$, and two different energy widths $E_{k_2} - E_{k_1} = 2.0$ MeV and 4.0 MeV, are compared to each other and to the weakly-bound orbitals for $E_B = 0.05$ MeV. The bin functions obtained with the weight factor $w_1(k)$ provide the closest match to the wave functions calculated in the weak-binding approximation. Overall, the different prescriptions for constructing bin functions result in large variations in the shape of the bin wave functions. The effects of these variations on inelastic scattering cross sections is studied in the next section.

3.4 Weak binding versus bin description: Scattering cross sections for selected single-nucleon particle-hole excitations

Inelastic scattering cross sections associated with the creation of particle-hole excitations depend on the radial wave functions of the single-nucleon hole and particle states. Here we investigate the sensitivity of the cross section to variations in the radial shape of the final (particle) state. We consider one-neutron transitions from an initial $1g_{9/2}$ orbital at $E_B(1g_{9/2}) = 12.37$ MeV to final resonance orbitals $1h_{9/2}$ at $E_B(1h_{9/2}) = $-5.28 MeV and $2f_{7/2}$ at $E_B(1h_{9/2}) = $-1.09 MeV. In both cases, we consider final ^{90}Zr states with $J^\pi = 3^-$.[2] Details of the calculations will be given in the next few sections.

In Figure 6 (top panel), we compare the results obtained with the weakly-bound wave functions, for various values of the binding energies, to each other and to the results obtained with bin wave functions. In the bottom panel of the figure, we show the effects of using different prescriptions for the bin functions

---

[2]Negative binding energies are used to indicate single-particle resonance energies: $E_{nlj}^{res} = -E_B(n,l,j)$.

on scattering cross sections. The calculations used the standard procedure for determining the bound-state function for the $1g_{9/2}$ orbital and employed the wave functions shown in the previous section for the $1h_{9/2}$ and $2f_{7/2}$ orbitals.

We observe that there is a strong dependence of the scattering cross section on the prescription used for the bin functions (see lower panels of Fig. 6). Furthermore, the magnitude of the cross section variation depends on the final state considered. For example, the cross sections at 5° vary by about a factor of two in the case that involves the $1h_{9/2}$ orbital and by more than an order of magnitude in the example that involves the $2f_{7/2}$ orbital. In contrast, the weak-binding results yield cross sections that vary very little for binding energies between $E_B = 4$ MeV and 0.05 MeV. This is not surprising given the results for the radial wave functions discussed in the previous section.

As mentioned above, a proper treatment of the continuum is not readily available for Surrogate applications and we have to resort to approximations. In particular, we assume that nucleons which are promoted to continuum states (via inelastic scattering) populate single-particle resonances. Here we have investigated the sensitivity of inelastic scattering cross sections to parameter variations in two possible descriptions of the resonance states. The bin description has exhibited much more sensitivity to the selected parameters than the weak-binding approach. While the bin description is conceptually attractive, it introduces additional uncertainties in the cross section calculations due to this parameter dependence. We thus choose to use the weak-binding approximation for calculating resonance wave functions in the remainder of this report.
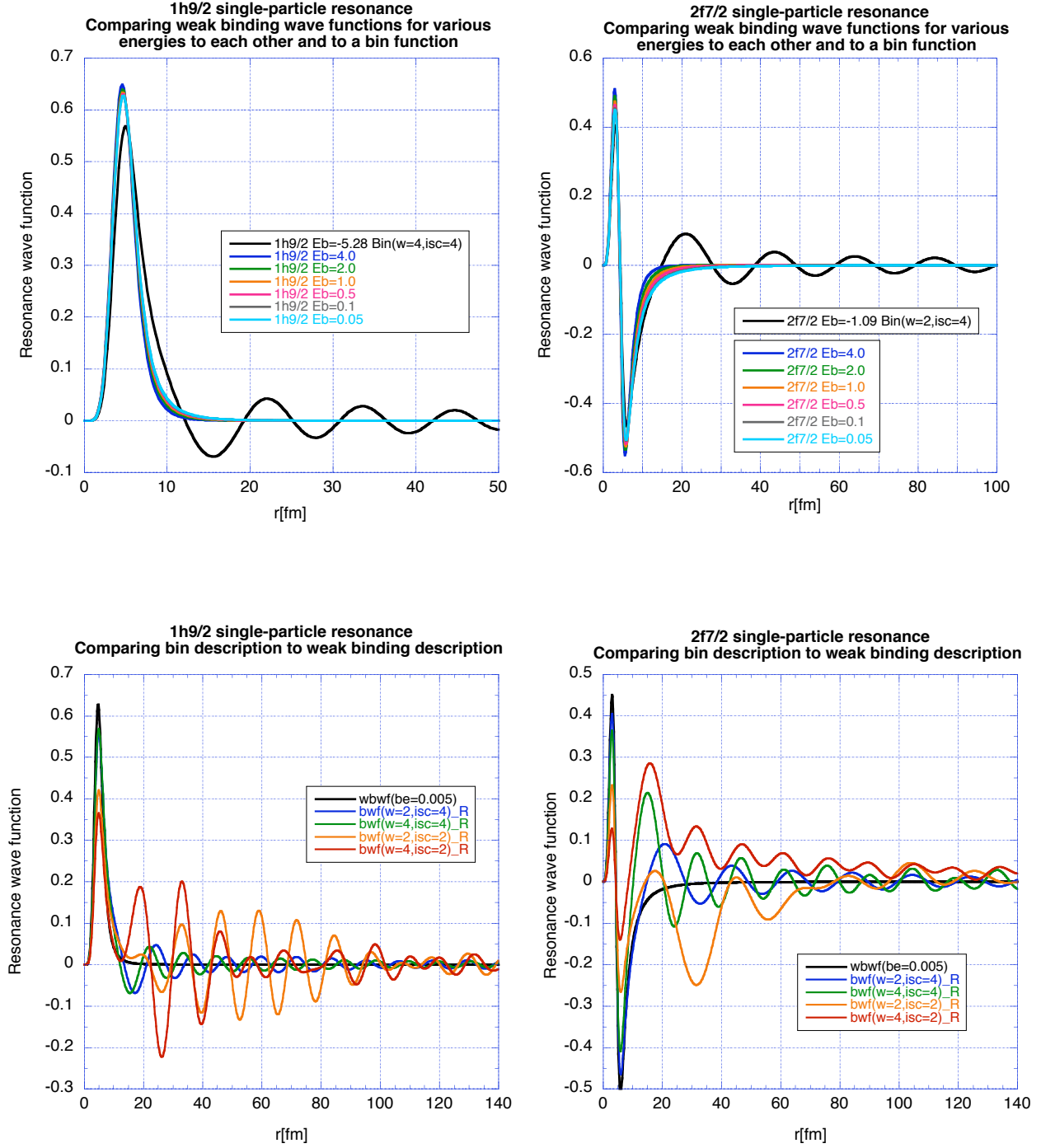
19

Figure 5: Radial single-particle resonance functions. Top panel: Wave functions obtained in the weak binding approximation for binding energies $E_B = 4.0$ MeV, 2.0 MeV, ..., 0.05 MeV, are compared to bin functions, calculated with the weight factor $w_1(k)$ (see text). Bottom panel: Bin wave functions, calculated with two different weight factors $w_1(k)$ (ISC=4) and $w_2(k)$ (ISC=2), and two different energy widths $E_{k_2} - E_{k_1} = 2.0$ MeV (w=2) and 4.0 MeV (w=4), compared to a weakly-bound wave function.
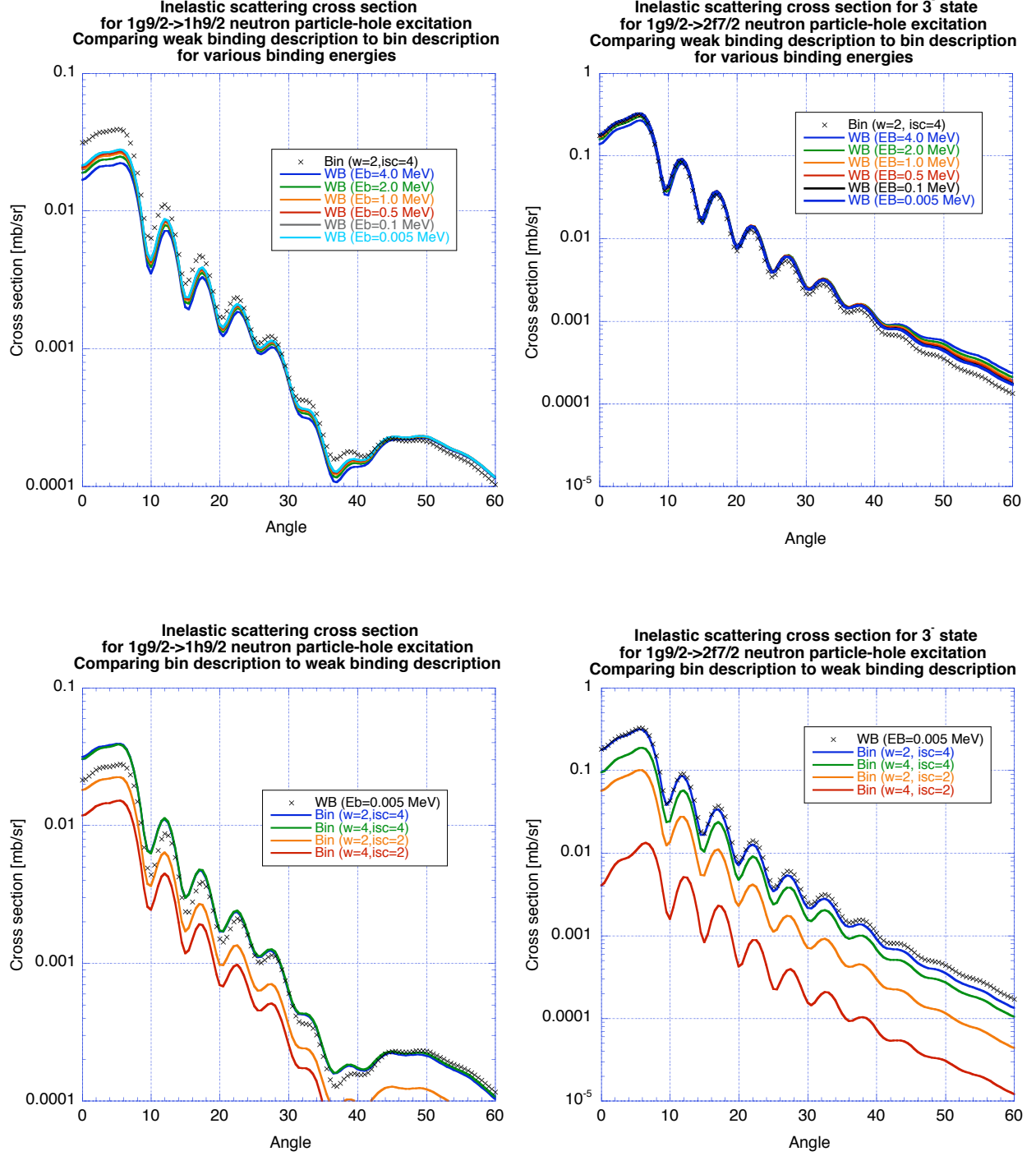
Figure 6: Inelastic scattering cross section for selected particle-hole excitations. Top panel: Cross sections obtained in the weak-binding approximation for $E_B = 4.0$ MeV, 2.0 MeV, ..., 0.05 MeV, compared to calculations using bin functions with the weight factor $w_1(k)$. Bottom panel: Cross sections obtained with bin wave functions, calculated with two different weight factors $w_1(k)$ (ISC=4) and $w_2(k)$ (ISC=2), and two different energy widths $E_{k_2} - E_{k_1} = 2.0$ MeV (w=2) and 4.0 MeV (w=4), compared to results from the weak-binding approximation.

21

4 Damping widths for particle-hole excitations

The model outlined in Section 2 requires that we determine the damping widths Γ_{m_h,m_p} of all particle-hole excitations that may contribute to the inelastic scattering cross section of interest. The damping widths of these states arise from their coupling to more complicated (2p-2h, etc.) configurations. It is this coupling that is driving the eventual formation of a compound nucleus.

The damping width of a given particle-hole excitation (m_h, m_p) can be related to the damping widths of the particle (m_p) and hole (m_h) states of which the excitation is composed [12]. In principle, one has to take into account possible correlations between the particle and the hole, especially in collective states. For our application we make the simplifying assumption that the particle and the hole decay independently of each other. This allows us to write the damping width as:

$$\Gamma_{m_h,m_p}(E_{m_h,m_p}) \quad = \quad \Gamma_{m_h}(E_{m_h}) + \Gamma_{m_p}(E_{m_p}) \, , \tag{18}$$

where $E_{m_h,m_p} = E_{m_h} + E_{m_p}$, and Γ_{m_p} and Γ_{m_h} denote the damping widths of the single-particle and single-hole states, respectively. Below we will determine the widths of the single-particle and single-hole states for the neutron and proton orbitals listed in Tables 1, 2, 4, and 5.

4.1 Single-particle damping widths

Empirical information on the widths of single-particle orbitals can be obtained from single-nucleon transfer (pickup and stripping) reactions and (direct) nucleon-scattering experiments [12, 59]. Comparisons of experimental and theoretically predicted single-particle damping widths provide also stringent tests of nuclear many-body theories. For practical applications, several analytic expressions, based on some underlying theoretical approach and developed to reproduce empirical results, can be found in the literature. The formulae express the widths as a function of the difference between the single-particle binding energy ($E_B = E_{m_h}$ or E_{m_p}) and the Fermi energy E_F, $E = E_B - E_F$:

1) The theory of infinite Fermi liquids predicts that the width should increase as the square of the energy (for low excitation energies), see Ref. [12], Equation (2):

$$\Gamma^{(IFL)} \quad = \quad aE^2 \text{MeV} \, . \tag{19}$$

   Bertsch $et\ al.$ [12] deduce an approximate proportionality constant of $a = \frac{1}{15}$ - $\frac{1}{20}$, based on available single-particle widths from experiments.

2) Brown and Rho [18] deduce the following expression

$$\Gamma^{(BR)} \quad = \quad 24 \frac{E^2}{E^2 + 500} \text{MeV} \, . \tag{20}$$

3) Jeukenne and Mahaux [49] suggest the following expression

$$\Gamma^{(JM)} \quad = \quad 18 \frac{E^4}{E^4 + 13.27^4} \text{MeV} \, . \tag{21}$$

4) Smith and Wambach [72] use the following expression

$$\Gamma^{(SW)} = 10.75 \frac{E^2}{E^2 + 18^2} \frac{110^2}{110^2 + E^2} \text{MeV} \, . \tag{22}$$

The last three expressions are taken from Brand $et\ al.$ [16], who compared the widths of spectral functions calculated in a Green-function approach to the analytic functions shown here.

In Figure 7 the analytic functions for the widths of the single-particle orbitals are shown as a function of the energy $E = E_B - E_F$. We select the prescription by Brown and Rho to determine the widths for the single-particle (bound and resonance) states considered in Section 3. The results are listed in Tables 6 and 7 for all relevant neutron and proton orbitals, respectively. The widths shown there will be used for the inelastic scattering calculations presented in this report.

Table 6: Quantum labels, energies and widths of relevant neutron orbitals in ^{90}Zr. "No." labels the single-particle neutron state for the potential under consideration. The quantum labels (l, j) give the orbital and total angular momentum values of the single-particle resonance and the label n enumerates the occurrence of the (l, j) quantum labels with increasing energy. E_B is the single-particle binding energy and Γ^{BR} is the width of the state as determined using the analytical formula based on the work by Brown and Rho.

No	orbital	n	l	j	E_B [MeV]	Γ^{BR} [MeV]
23	$1j_{15/2}$	1	7	7.5	-18.200	14.646
17	$1i_{11/2}$	1	6	5.5	-15.480	13.456
16	$1i_{13/2}$	1	6	6.5	-7.8500	9.2001
11	$1h_{9/2}$	1	5	4.5	-5.2800	7.4894
13	$2f_{5/2}$	2	3	2.5	-2.8900	5.8327
12	$2f_{7/2}$	2	3	3.5	-1.0900	4.5875
10	$1h_{11/2}$	1	5	5.5	3.1450	1.9421
8	$1g_{7/2}$	1	4	3.5	4.9950	1.0509
9	$2d_{3/2}$	2	2	1.5	5.1530	0.98544
7	$3s_{1/2}$	3	0	0.5	5.9895	0.67039
6	$2d_{5/2}$	2	2	2.5	7.1945	0.31664
5	$1g_{9/2}$	1	4	4.5	12.370	0.31765
4	$2p_{1/2}$	2	1	0.5	13.080	0.51149
3	$2p_{3/2}$	2	1	1.5	14.110	0.86730
2	$1f_{5/2}$	1	3	2.5	14.880	1.1866
1	$1f_{7/2}$	1	3	3.5	20.990	4.8202

Table 7: Quantum labels, energies and widths of relevant proton orbitals in ^{90}Zr. The labels are the same as in Table 6.

| No	orbital	n	l	j	E_B [MeV]	Γ^{BR} [MeV]
26	$1j_{15/2}$	1	7	7.5	-24.73	15.953
20	$1i_{11/2}$	1	6	5.5	-21.83	14.889
21	$2g_{9/2}$	2	4	4.5	-18.23	13.326
19	$1i_{13/2}$	1	6	6.5	-14.14	11.187
14	$1h_{9/2}$	1	5	4.5	-11.43	9.5539
16	$2f_{5/2}$	2	3	2.5	-9.81	8.5037
17	$3p_{3/2}$	3	1	1.5	-9.24	8.1232
15	$2f_{7/2}$	2	3	3.5	-7.18	6.7131
13	$1h_{11/2}$	1	5	5.5	-3.78	4.3592
12	$2d_{3/2}$	2	2	1.5	-1.22	2.7080
10	$1g_{7/2}$	1	4	3.5	0.34	1.8016
9	$2d_{5/2}$	2	2	2.5	1.30	1.3273
8	$1g_{9/2}$	1	4	4.5	5.11	0.12228
7	$2p_{1/2}$	2	1	0.5	8.3545	0.12227
6	$2p_{3/2}$	2	1	1.5	10.40	0.62142
5	$1f_{5/2}$	1	3	2.5	10.80	0.76071
4	$1f_{7/2}$	1	3	3.5	17.00	4.1644
3	$2s_{1/2}$	2	0	0.5	21.80	7.4795
2	$1d_{3/2}$	1	2	1.5	23.80	8.8207
1	$1d_{5/2}$	1	2	2.5	23.80	8.8207
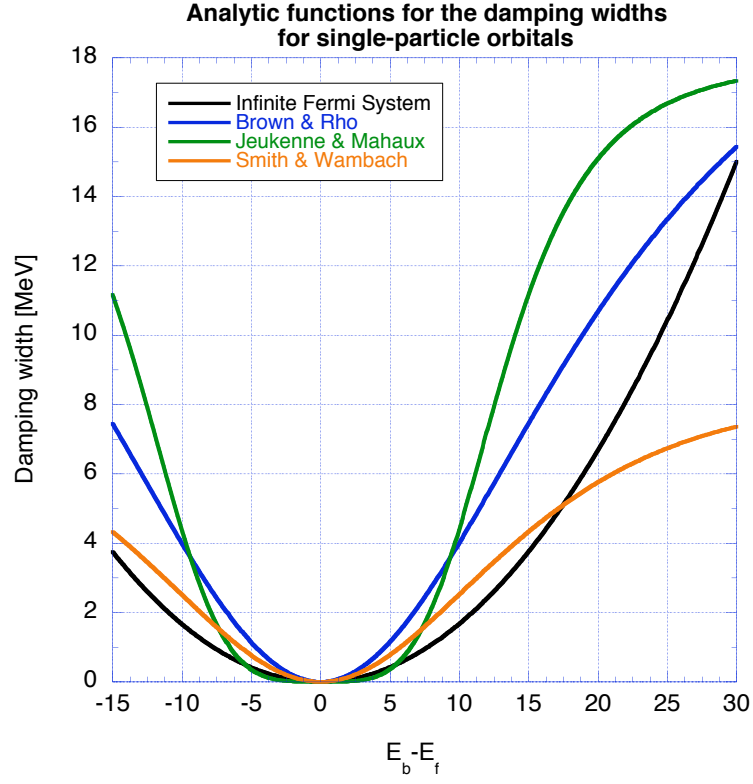
Figure 7: Analytic functions for the damping widths of the single-particle orbitals in ^{90}Zr, as a function of the difference between the single-particle binding energy and the Fermi energy. Four different theoretical prescriptions have been employed (see text).

5 The Projectile-Target Interaction

Calculations of cross sections for direct reactions involving α particles require α-nucleus optical potentials. Knowledge of these potentials is important for a variety of processes, such as elastic and inelastic scattering, transfer reactions, and radiative capture, involving a variety of targets and a wide range of energies. Phenomenological α-nucleus potentials [61, 4, 55], as well as semi-microscopic potentials, based on a single-folding [56, 48, 53] or double-folding [71, 51, 52, 2, 50] procedure, have been used over the years.

In the model employed here, ^{90}Zr target excitations are induced via an inelastic scattering process in which the α projectile interacts with the individual target nucleons, thus producing some superposition of 1-particle 1-hole excitations. The formalism outlined in Section 2 requires that the interaction of the projectile with the nucleon which is involved in a particular particle-hole transition is taken into account as well as the interaction of the projectile with the remaining 'core' (^{89}Zr or ^{89}Y here). Furthermore, we need the interaction of the projectile with the target nucleus (^{90}Zr) as a whole in order to calculate the distorted waves in the incoming and outgoing channels.

In a rigorous microscopic approach, one would start from a nucleon-nucleon force and obtain the α-nucleon interaction via a single-folding procedure (integrating over the volume of the α-particle) and the α-nucleus interaction via a double-folding procedure (integrating over the volumes of both the α-particle and the target nucleus). However, since the inelastic scattering calculations presented in this report require α-nucleus potentials for the target nuclei ^{89}Y , ^{89}Zr , ^{90}Zr , ^{91}Zr , ^{91}Nb , for a wide range of energies, ranging from tens of MeV to more than 100 MeV, we find it advantageous to make use of a phenomenological optical potential with an analytic energy dependence. We employ the global optical potential by Avrigeanu *et al.* [61, 4]. The form of the Avrigeanu potential is given in Section 5.1 below and elastic scattering cross sections calculated with this potential are compared to experimental results in Section 5.2.

For the effective α-nucleon interaction, we employ an energy- and densitiy-independent Gaussian form. Possible parametrizations for the Gaussian are given in Section 5.3 and the sensitivity of selected calculated inelastic scattering cross sections to the parameter choices is discussed in Section 5.4.

5.1 The α-nucleus optical potential by Avrigeanu *et al.*

In 1987, Nolte *et al.* [61] derived a set of parameters for a global optical potential from α-nucleus scattering with energies higher than 80 MeV. The authors employed the (Wood-Saxon) geometry and energy dependence of an optical model introduced earlier by Put and Paans [64, 65] and compared their optical-model predictions to elastic and inelastic scattering data. In 1994, Avrigeanu, Hodgson, and Avrigeanu [4] extended the potential for lower energies in order to describe (n, α) reactions. They found good agreement with the experimental data for (n, α) reactions on a variety of nuclei in the mass region $A = 48$–59.

The global optical α-nucleus potential of Avrigeanu *et al.* has the form:

$$U^{AHA}_{\alpha-nucleus}(r) \quad = \quad V_C(r) - V_\alpha \frac{1}{1 - \exp\left(\frac{r - R_v}{a_v}\right)} - iW_\alpha \frac{1}{1 - \exp\left(\frac{r - R_w}{a_w}\right)} \ , \tag{23}$$

where $R_x = r_x A^{1/3}_{target}$ and a_x $(x = v, w)$, are the radii and the diffuseness parameters of the potential wells, and $V_C(r)$ is the Coulomb potential. The strengths of both the real and the imaginary components depend linearly on the energy of the α particle. In addition, the depth of the real potential depends on $Z/A^{1/3}$ while the depth of the imaginary term scales with $A^{1/3}$. The radii remain fixed, while the diffuseness parameters decrease with increasing target size as $\propto A^{1/3}$. The parametrization for energies below as well as above 73 MeV are shown in Table 8.

5.2 Elastic α-scattering results compared to experimental data

To test the optical potential $U^{AHA}_{\alpha-nucleus}(r)$, we have calculated elastic scattering cross sections for $\alpha + ^{90}$Zr for various projectile energies. In Figure 8, we compare the cross sections to the experimental results by Put and Paans [64, 65] (as given in the EXFOR database at the NNDC). The calculations show good agreement with the experimental data, in particular for energies larger than 70 MeV. For more accurate calculations at lower energies, it might be worthwhile investigating the potential by Atzrott *et al.* [2], which is based on a

Table 8: Parametrization of the global α-nucleus potential by Avrigeanu, Hodgson, and Avrigeanu [4].

Parameter	Value
V_α [MeV]	$101.1 + 6.051 \cdot Z/A^{1/3}$ - 0.248 E_α
r_v [fm]	1.245
a_v [fm]	$0.817 - 0.0085 \cdot A^{1/3}$
W_α [MeV]	$12.64 - 1.706 \cdot A^{1/3} + 0.200\ E_\alpha$; $E_\alpha < 73$ MeV
	$28.82 - 0.006 \cdot A^{1/3} + 0.200\ E_\alpha$; $E_\alpha > 73$ MeV
r_w [fm]	1.570
a_w [fm]	$0.692 - 0.02 \cdot A^{1/3}$
r_C [fm]	1.240

double-folding approach. Since we are primarily concerned with incoming α particles with energies around 100 MeV, we will use the potential by Avrigeanu *et al.* in the remainder of this report.

5.3 The effective α-nucleon interaction

Here we are concerned with the contribution of the projectile-nucleon interaction to the scattering cross section. The goal is to calculate the matrix elements of Equation 13 for specific particle-hole excitations of the target. To this end, an expression for the projectile-nucleon interaction $V_{\alpha n}(r) = V(|\vec{r}_\alpha - \vec{\xi}|)$ is required, where $r = |\vec{r}_\alpha - \vec{\xi}|$ is the distance between the nucleon and the center of mass of the projectile. Since we are interested in the interaction of the alpha particle with a nucleon inside a nucleus, rather than in free alpha-nucleon scattering, we require an effective interaction. We will focus on the form of the alpha-neutron interaction and simply add a Coulomb term for the alpha-proton interaction.

The most popular form for the effective alpha-nucleon interaction is an energy- and density-independent Gaussian function. Arguments that lead to this form for the interaction are given in Ref. [7], where A.M. Bernstein obtains the α-nucleon potential by averaging the nucleon-nucleon interaction over the size of the α particle using Gaussian shapes for the nn interaction and for the α-particle wave function. Early forms of the effective alpha-nucleon interaction were purely real [7, 6], while the newer forms, such at those of Refs. [10, 69, 68, 56], include a complex component that usually has the same shape and range as the real part:

$$\begin{aligned} V_{\alpha n}(r) &= -V_{\alpha n}^0 \exp(-K^2 r^2) & (24) \\ V_{\alpha n}^0 &= v_0 + i w_0 & (25) \end{aligned}$$

Typically, the interaction $V_{\alpha n}(r)$ is folded with the density of a target nucleus to produce an optical α-nucleus potential that is appropriate for cross section calculations for elastic or inelastic α scattering.

Many authors have employed the $V_{\alpha n}(r)$ parametrization introduced by Bertrand *et al.* [10], who studied measurements of giant monopole and quadrupole resonances for ^{208}Pb, ^{120}Sn, ^{90}Zr , ^{58}Ni, and ^{46}Ti, using inelastic scattering of 152-MeV α particles. In Ref. [10], experimental results were compared to DWBA calculations as well as to folding-model calculations, using Tassie transition densities and an effective α-nucleon interaction. For each target considered, optimal strength values v_0 and w_0 were determined for various range parameters $\mu = K^{-1}$ by fitting the calculations to elastic scattering data at small scattering angles θ. Best values for μ were then obtained by carrying out χ^2-fits. Essentially the same optimal value for the range parameter, namely $\mu = 1.94$ fm, was found for all target nuclei, see Figure 6 of Ref. [10]. The strengths parameters v_0 and w_0 determined in this manner for the different nuclei are listed in Table III of Ref. [10]. For ^{90}Zr the authors obtained $v_0 = 36.4$ MeV and $w_0 = 21.1$ MeV. Parameters based on the Bertrand prescription were adopted by Satchler *et al.* [69, 68] in subsequent studies of inelastic alpha scattering on several spherical nuclei.

Another popular parametrization was introduced in 1994 by Lund *et al.* [56], who studied the isospin character of transitions to low-lying collective states in ^{90,92,94,96}Zr from the ground states of the respective nuclei. Their article reports on measurements of elastic and inelastic scattering of 35.4 MeV alpha particles.

The data were analyzed using a deformed optical-model potential and a folding model, assuming transition densities of the standard collective type and resulting from RPA calculations, respectively. Fitting the calculations to the elastic scattering data resulted in $v_0 = 49.736$ MeV and $w_0 = 16.774$ MeV for the ^{90}Zr case. Parameters for other zirconium isotopes are given in Table V of Ref. [56]. The range parameter was kept fixed at $\mu = 1.94$ fm.

A range parameter of $\mu = K^{-1} = 1.94$ fm has been seen to work well in many applications, so a standard procedure is to use this value and to adjust the strengths v_0 and w_0 to reproduce the data of interest. It should be noted, though, that there is currently not enough information available to uniquely determine a set of optimal parameters for the α-nucleon interaction. For example, the choice of $\mu = 1.94$ fm is based on the experience that this value represents a good average of ranges required to produce folding potentials for the description of elastic α-nucleus scattering data. However, a different parameter combination can produce a similarly successful fit to elastic data, while resulting in an increase or decrease of the calculated inelastic cross sections. This issue has been discussed by Horen *et al.* [48] and deserves further study. In addition, it is possible to employ different range parameters for the real and imaginary parts of the interaction and/or to consider a density-dependent form for the α-nucleon interaction, as was done, e.g., by Satchler and Khoa [70], as well as by Kolomiets *et al.* [53].

In the present work, we will employ an energy and density-independent Gaussian function to represent the effective projectile-nucleon interaction. In the next section, we will investigate the dependence of the inelastic scattering cross section on the parameters chosen for the Gaussian. Specifically, we will present cross section calculations for selected neutron particle-hole transitions leading to excited ^{90}Zr states with various $J\pi$ values.

5.4 Sensitivity of the scattering cross sections to the parameter choice for the projectile-nucleon interaction

Here we investigate how varying the parameters of the effective alpha-nucleon interaction $V_{\alpha n}(r)$ will affect the inelastic alpha-nucleus scattering cross sections. We focus on a particular particle-hole excitation induced in ^{90}Zr by alpha scattering, namely the transition of a neutron from a bound 1g9/2 orbital to a bound 1h11/2 orbital. The resulting target excitation has an energy of 9.2247 MeV and can have total angular momentum and parity values $J\pi = 1^-, 3^-, 5^-, 7^-$, and 9^-. We will consider parametrizations employed by Bertrand [10], Lund [56], and Horen [48]. The former two have the same Gaussian shape, characterized by a range parameter fixed at $\mu = 1.94$ fm, but different strength parameters v_0 and w_0. Horen *et al.* have not only varied the strengths of the real and imaginary parts of $V_{\alpha n}(r)$, but have also considered adjusting the range parameter. In order to study the effect of the range parameter, we select one of the parameter sets employed in Ref. [48], namely, $\mu = 1.82$ fm, $v_0 = 88.200$ MeV, and $w_0 = 10.900$ MeV.

Figure 9 shows calculated inelastic-scattering cross sections for $J\pi = 1^-, 3^-, 5^-$, and 7^-. Each panel gives results for the three parametrizations considered. We observe that varying the parameters has a clearly visible effect on the resulting cross sections. For $J > 1$, the cross sections seem to differ by an overall factor, while for $J = 1$, both the magnitude and the shape of the cross section changes, in particular for angles between 20 and 40 degrees.

An overall rescaling of the individual cross sections will affect the total inelastic scattering cross section that remains to be calculated, but not the predicted $J\pi$ distribution of the excited target. To investigate this issue further, we have plotted ratios of the individual cross sections for different parameter choices. The top panel of Figure 10 gives the cross sections obtained with the Bertrand parameters divided by the relevant cross sections obtained with the Lund parameters, for $J\pi = 1^-, 3^-, 5^-$, and 7^-. The ratios for angular momenta larger than one are constant across the angular range considered and agree with each other. The behavior of the $J\pi = 1^-$ curve, on the other hand, is clearly different. The bottom portion of the figure shows analogous ratios with respect to the Horen parametrization, namely $\sigma(\text{Bertrand})/\sigma(\text{Horen})$ on the left and $\sigma(\text{Lund})/\sigma(\text{Horen})$ on the right. We observe that the ratios for the $J > 1$ cases essentially agree with each other in their angular dependence, but differ in their absolute values. The $J\pi = 1^-$ curve is again very different from the other cases.

The behavior of the curves in Figure 10 can be understood by considering the different contributions to the inelastic scattering cross sections studied here. Figure 11 shows the results of calculations for which either the alpha-nucleon interaction or the alpha-core interaction has been set to zero. The lower right panel

shows cross sections that contain only the alpha-core contributions: The solid line refers to the $J\pi = 1^-$ case, while the dashed, short-dashed, and dotted lines (see insert) refer to $J\pi = 3^-, 5^-$, and 7^-, respectively. The other three panels show cross sections that contain only the alpha-nucleon contributions: The $J\pi = 1^-, 3^-$, and 5^- cases are shown in the top left, top right, and bottom left panels of the figure. Here, the solid, dashed, and dotted lines correspond to the Horen, Lund, and Bertrand parameter sets, respectively. We observe that the cross sections drop off with increasing angular momentum. While the cross section due to the alpha-nucleon interaction decreases moderately with increasing J value, the drop in the alpha-core cross section is quite dramatic: Where the former decreases by an order of magnitude, the latter drops by 6-8 orders of magnitude. Consequently, the contributions due to the alpha-core interaction can be neglected in all but the $J\pi = 1^-$ case, where both parts of the projectile-target interaction contribute equally to the overall cross section and produce interference effects. The fact that the alpha-core interaction is only significant for $J\pi = 1^-$ and becomes negligible for larger J values has also been demonstrated analytically in the PWBA approximation [25].

The Bertrand and Lund parametrizations of $V_{\alpha n}(r)$ differ in the strengths parameters v_0 and w_0 only. Since the scattering cross sections are proportional to the square of the matrix element μ_{m_h, m_p} (see Equation 14), we see that for situations in which the core contributions are negligible, the cross section ratio is $\sigma(Bertrand)/\sigma(Lund) = [(v_0^{(B)})^2 + (w_0^{(B)})^2]/[(v_0^{(L)})^2 + (w_0^{(L)})^2] = 0.5914$, where the superscripts (B) and (L) refer to the Bertrand and Lund parametrizations, respectively. The numerical value of this ratio agrees with the ratio shown in the top panel of Figure 10 for $J\pi = 3^-, 5^-$, and 7^-. This result is independent of angular momentum.

The Horen parametrization contains a range parameter that differs from the one used by Bertrand and Lund. Changing the range parameter affects the inelastic cross sections in a manner that depends on the angular momentum of the final state, as can be inferred from the bottom panels of Figure 10 for $J\pi = 3^-, 5^-$, and 7^-. Hence it will be useful study the dependence of the final $J\pi$ distribution following inelastic alpha scattering on the range parameter employed in the calculation.

Due to the interference of the contributions from the alpha-nucleon interaction with the contributions arising from the alpha-core interaction, the $J\pi = 1^-$ inelastic scattering cross section is very sensitive to the parametrization selected for $V_{\alpha n}(r)$ (see Figure 10 as well as the top left panel of Figure 9). Consequently, cross section predictions for this angular-momentum value should be regarded with some caution. A comparison of a cross section calculation carried out in the formalism employed in this report with a calculation based on transition densities obtained from an RPA approach is expected to provide further insights [26, 32].

Throughout the remainder of this document, we will employ the Lund parametrization for the α-nucleon interaction.
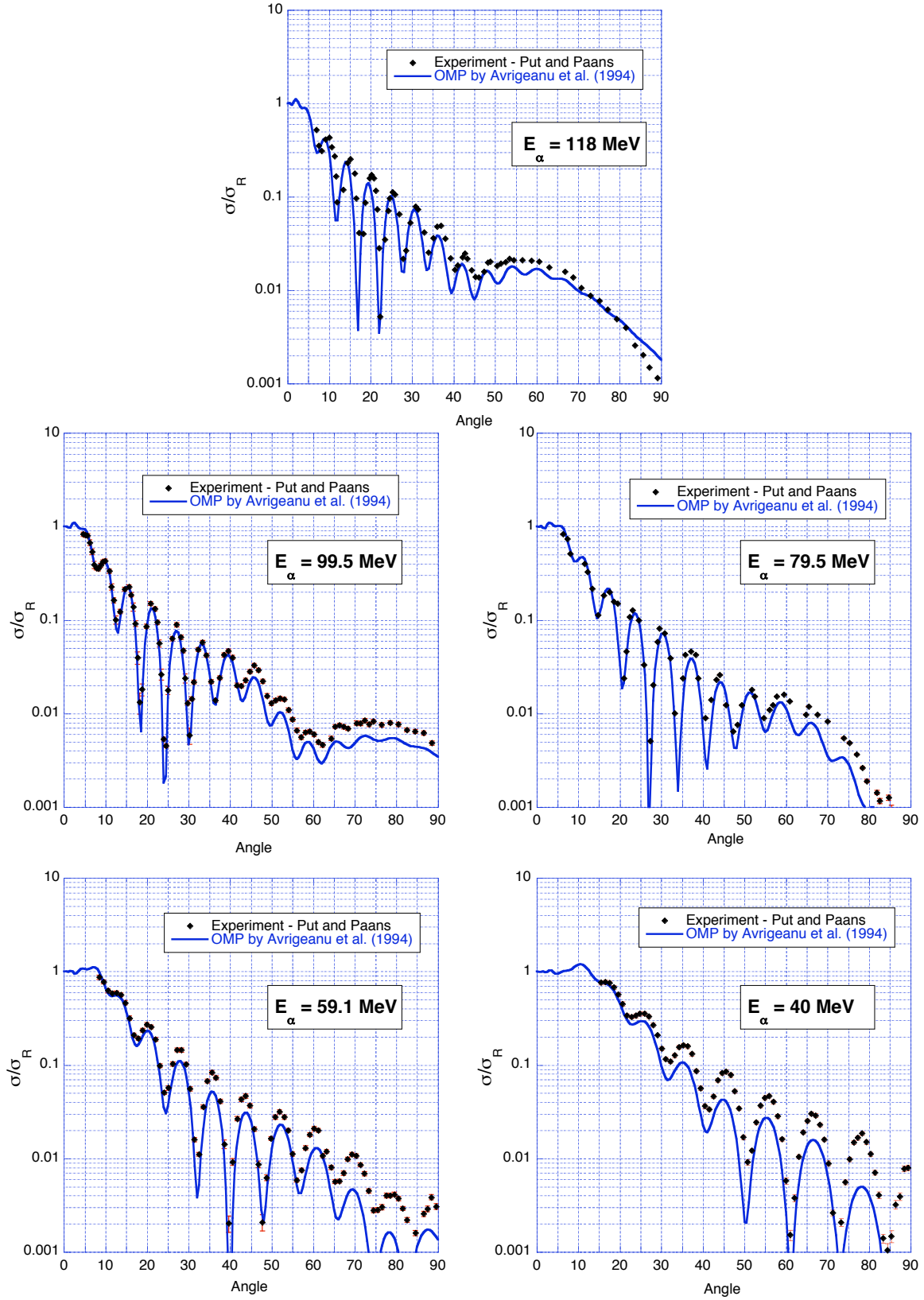
Figure 8: Elastic scattering cross sections for $\alpha + {}^{90}\text{Zr}$, for various projectile energies. The experimental results are taken from Put and Paans [64, 65].
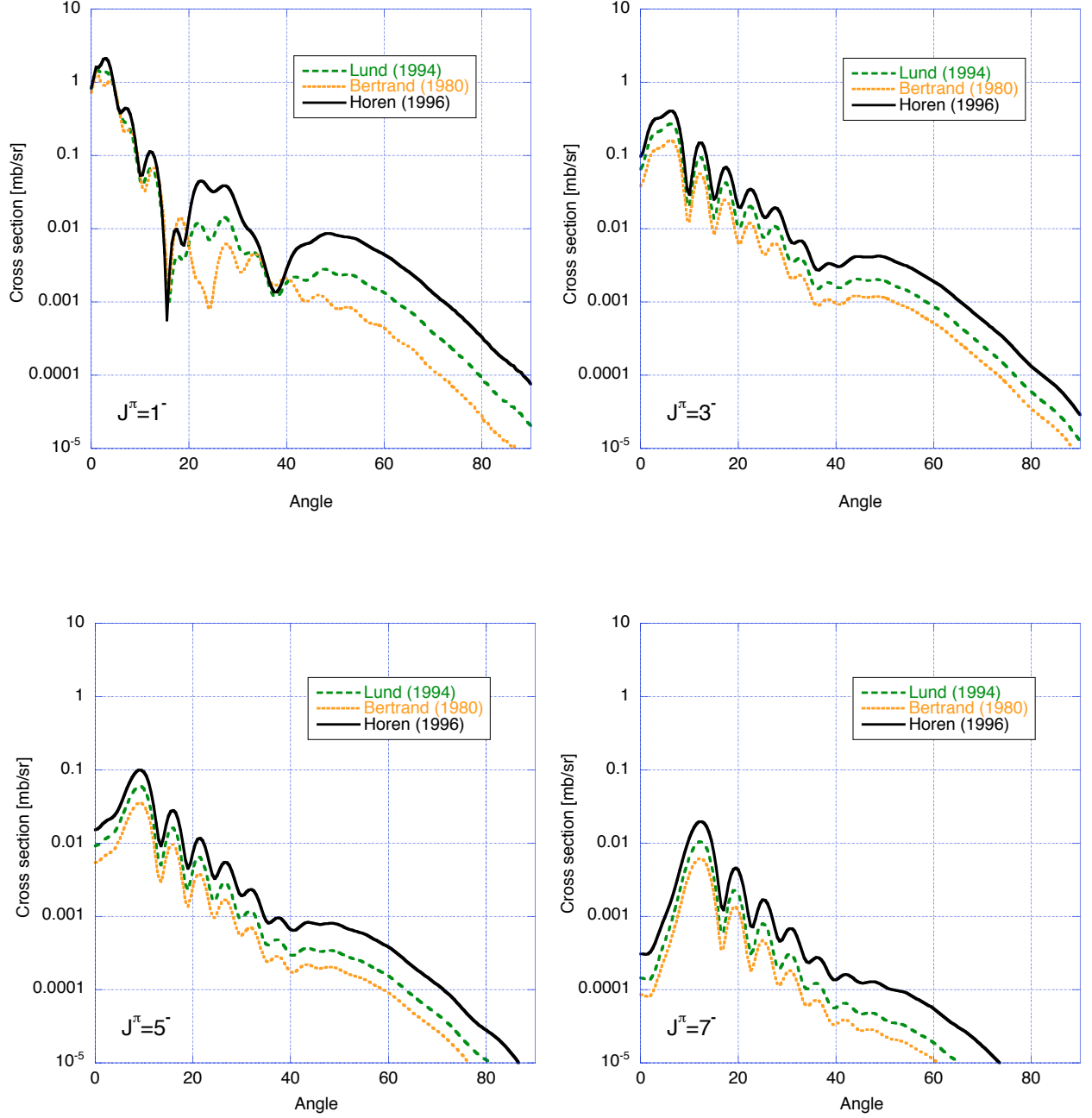
Figure 9: Cross sections for inelastic scattering of 140 MeV alpha particles from ^{90}Zr . The calculations show results for a process in which a target nucleon makes a transition from a 1g9/2 orbital to a 1h11/2 orbital. Final target states with E_{ex}=9.22 MeV and $J\pi = 1^-, 3^-, 5^-$, and 7^- are studied and three different parametrizations of the alpha-nucleon interaction are considered.
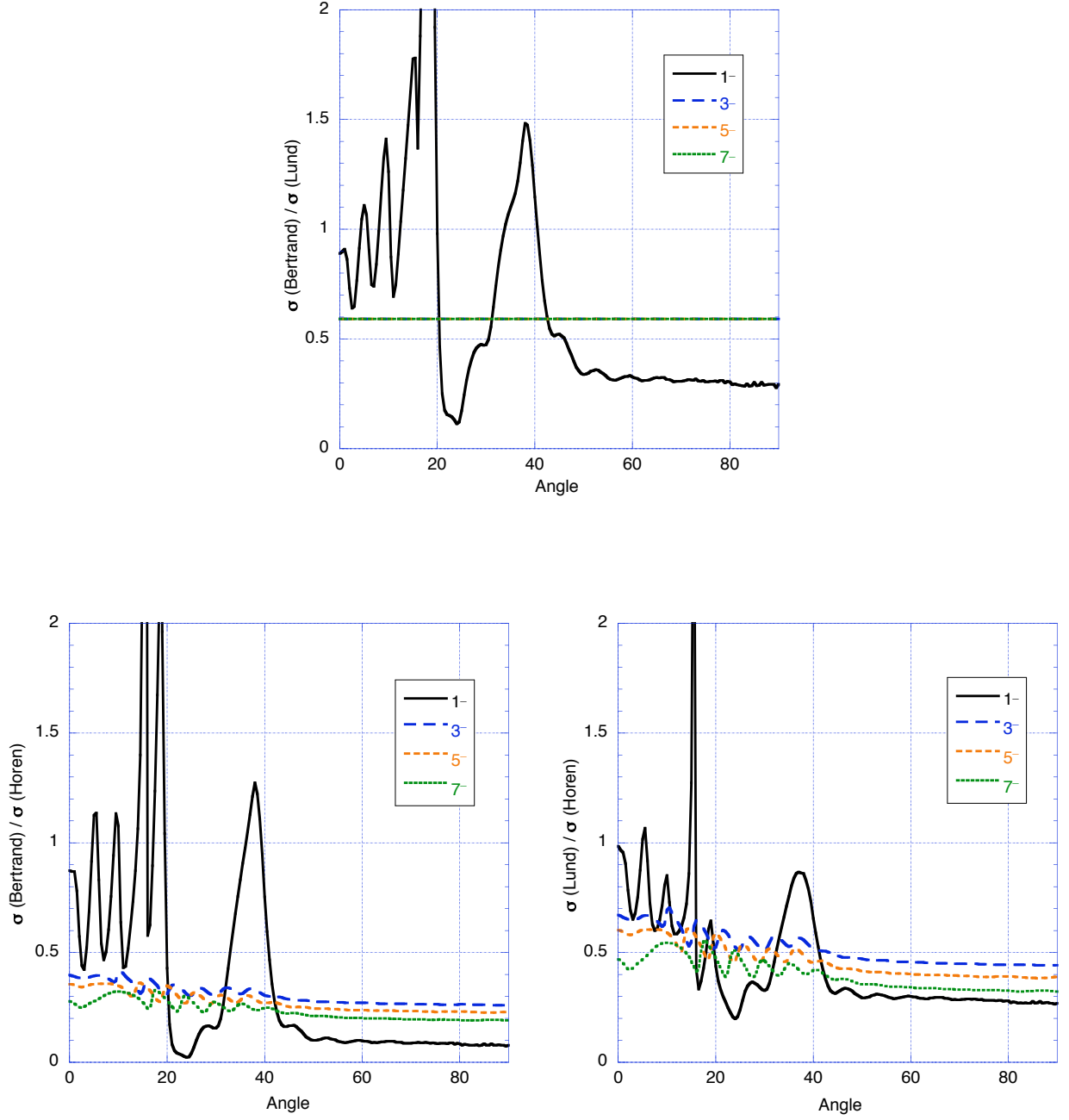
Figure 10: Cross section comparisons for different parameterizations of the alpha-nucleon interaction. Shown are the cross section ratios $\sigma(\text{Bertrand})/\sigma(\text{Lund})$, $\sigma(\text{Bertrand})/\sigma(\text{Horen})$, and $\sigma(\text{Lund})/\sigma(\text{Horen})$ for $J\pi = 1^-, 3^-, 5^-,$ and 7^-. The cross sections entering the ratios are those shown in the previous figure.

31
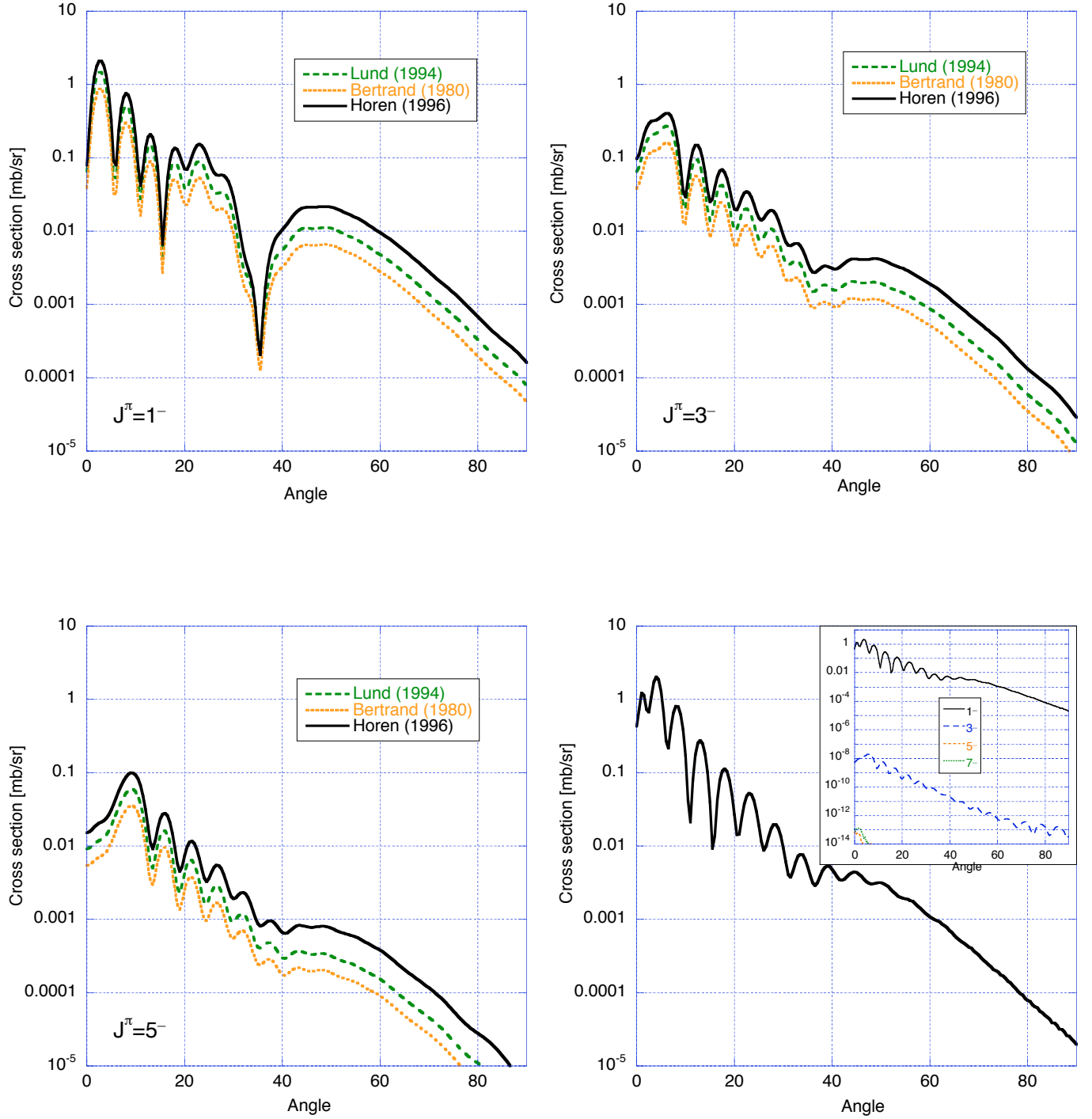
Figure 11: Contributions to the inelastic scattering cross section arising from the alpha-nucleon and alpha-core interactions. The process is the same as in Figure 9. The lower right panel shows cross section calculations that contain only the alpha-core contributions, while the other panels show cross section calculations that contain only the effects of the alpha-nucleon interaction. For the latter case, three different parameter sets have been considered (Lund, Bertrand, Horen).

6 Scattering Cross Sections for Individual Particle-Hole Excitations

The model employed in this work assumes that the inelastic scattering cross section for $^{90}\text{Zr}(\alpha,\alpha')^{90}\text{Zr}^*$ can be expressed in terms of cross sections for producing uncorrelated particle-hole excitations in the target nucleus. Specifically, the cross section is given as an incoherent sum of scattering cross sections $(\frac{d\sigma}{d\Omega})_{m_h,m_p}$ for individual particle-hole excitations (m_h, m_p) with weights $|a(m_h, m_p)|^2$ that depend on the energy and spreading widths of the particle-hole configurations (see Eq. 12 in Sect. 2.3). Below, we will show the distribution of the neutron and proton particle-hole excitations generated in the model across an energy range of $E_{ex} = 5 - 23$ MeV for the target nucleus $^{90}\text{Zr}^*$. We will illustrate the effect of the spreading, and present the scattering cross sections associated with the individual particle-hole excitations. In the next section, we will employ these ingredients to generate total elastic scattering cross sections for various energies and show the contributions to the total cross section associated with different $J\pi$ values in the compound nucleus.

6.1 Distribution of particle-hole states

Using the single-nucleon orbitals listed in Table 6 (for neutrons) and Table 7 (for protons) as a starting point, all possible particle-hole states were constructed by considering all allowed transitions from an occupied (hole) orbit to an unoccupied (particle) orbit. For the target under consideration, ^{90}Zr, we assumed that each orbital is either fully occupied or completely empty. A generalization to partially occupied levels is straightforward. For each particle-hole state the appropriate energy and spreading width were calculated and the possible angular-momentum and parity values were determined. The resulting distributions of uncorrelated particle-hole excitations are shown in Figure 12, arranged according to their $J\pi$ values and given as a function of the ^{90}Zr excitation energy. Neutron particles-hole excitations are shown in black, proton excitations are given in red. Only states in the energy range 5-23 MeV are shown. The plot shows that for most energy regions, a range of angular-momentum and parity values can be populated. Around $E_{ex} \approx 10$ MeV, e.g., negative-parity states are seen to dominate, while around 15 MeV there is a more even distribution of positive and negative parity states.

Incorporating many-body correlations in the description of the structure of the ^{90}Zr target will affect the energy of each particle-hole configuration and, moreover, will spread it over many excited many-nucleon states that lie within several MeV of the energy of the uncorrelated state. The effect of the spreading is accounted for via the approach described in Sections 2.3. It involves folding the cross sections for the individual particle-hole excitations with Lorentzian distributions that approximate the effect of the many-body correlations and that have widths which were determined in Section 4. The effect of the spreading is illustrated in Figure 13 for negative parity states and the individual cross sections are discussed next.

6.2 Cross sections for particle-hole excitations (Lund parametrization)

The cross sections for exciting the individual particle-hole excitations are shown in Figures 14–17. The cross section results are grouped by the $J\pi$ values of the excited ^{90}Zr state. Figures 14 and 15 display cross sections for neutron particle-hole excitations for positive-parity and negative-parity states in ^{90}Zr , respectively, while Figures 16 and 17 show results for proton particle-hole excitations leading to positive-parity and negative-parity states, respectively.

We observe that for a given $J\pi$ combination, the cross sections have a characteristic shape, but differ in magnitude by as much as a factor of 100. With increasing J value (which here corresponds to the angular-momentum transfer l since we consider scattering of a spin-zero projectile from a spin-zero target), the location of the first maximum moves to larger angles - a feature that is in line with an approximate description of the scattering process in the Fraunhofer picture (strong absorption limit). This is also illustrated in Figure 18, where the relationship between the angular momentum J and the location of the first scattering maximum is plotted. We furthermore observe that, on average, the cross sections decrease with increasing angular-momentum transfer.

Plotting the individual cross sections is not only instructive, it also serves the purpose of testing the convergence of the calculations: The individual scattering cross sections can be obtained using various

choices of the parameters that determine the details of the calculations, such as step sizes for integrations. One of the signs that a calculation has not converged (for a particular energy or angular range) is the occurrence of unexpected features on the calculated cross sections. An example of this can be seen in the $J\pi=6^+$ panel of Figure 14: At large angles, around 85°-90° a few of the calculated cross sections exhibit small "noise". The effects for the case shown here have not been corrected for since they are very minor and will not affect the final results.
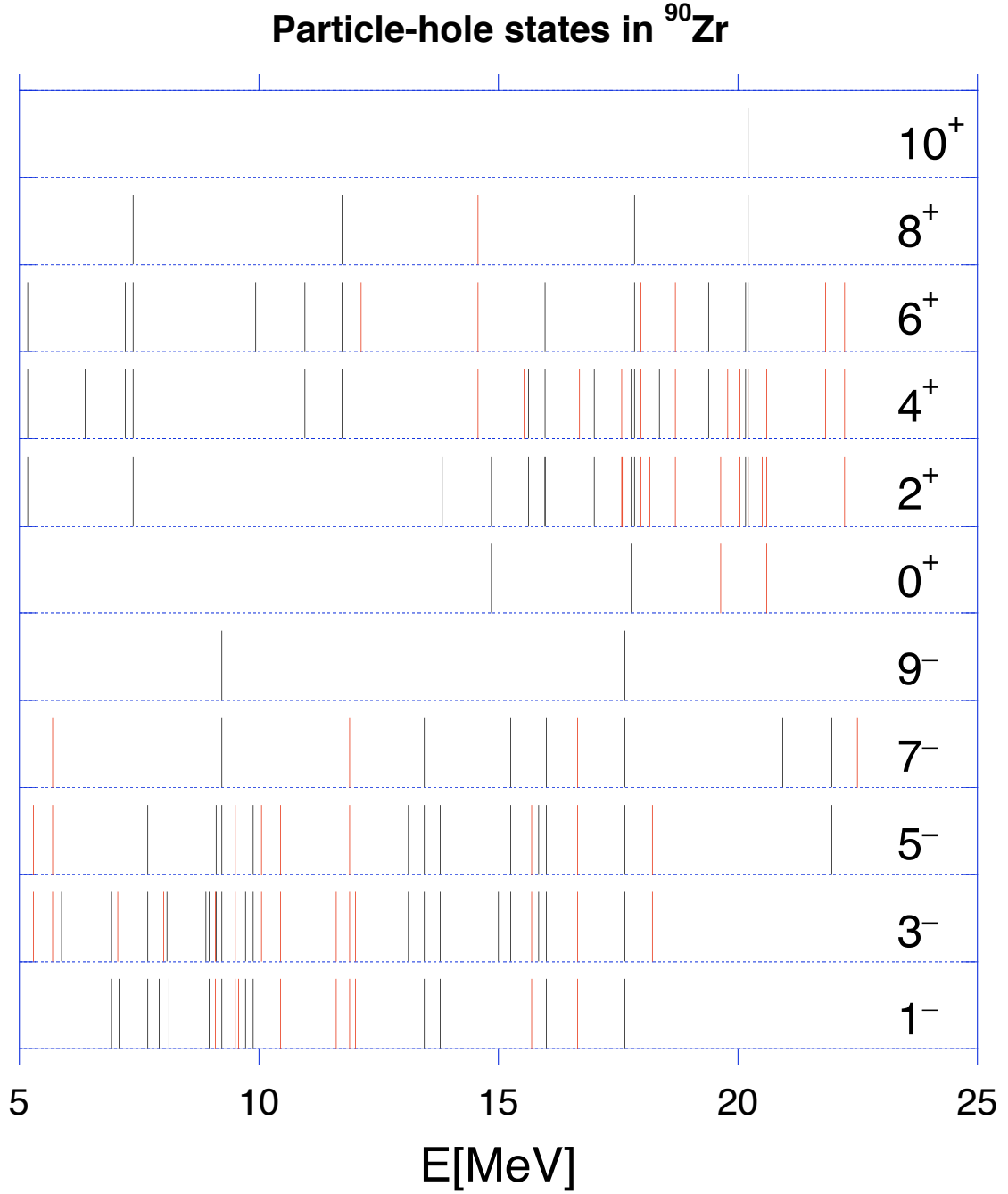
Figure 12: Energy distribution of uncorrelated particle-hole excitations in ^{90}Zr. Shown are the energies of all particle-hole states considered in our study. Neutron (proton) particle-hole states are given in black (red) and the total angular momentum and parity of the excited ^{90}Zr final state are indicated on the right side within each panel. Cross sections for inelastic scattering to the states displayed here were calculated and are shown below.
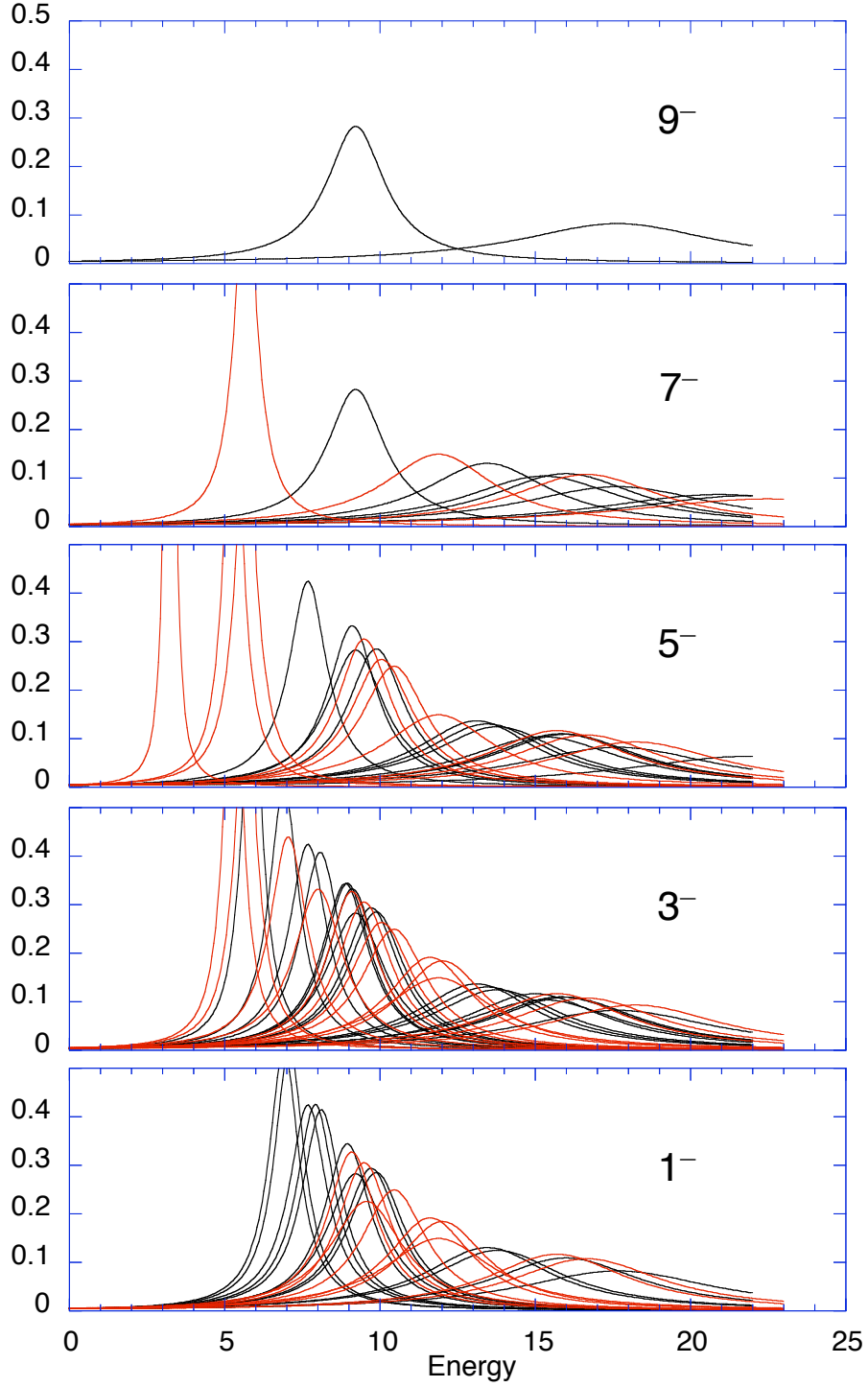
Figure 13: "Smeared" energy distributions of negative-parity particle-hole excitations in ^{90}Zr. Shown are Lorentzian shapes which approximate the energy spreading of particle-hole states due to residual many-body effects. All negative-parity states with $E_{ex} > 5.0$ MeV are shown. Neutron (proton) particle-hole states are given in black (red) and the total angular momentum and parity of the excited ^{90}Zr final state are indicated on the right side within each panel. Compare also to Figure 12.
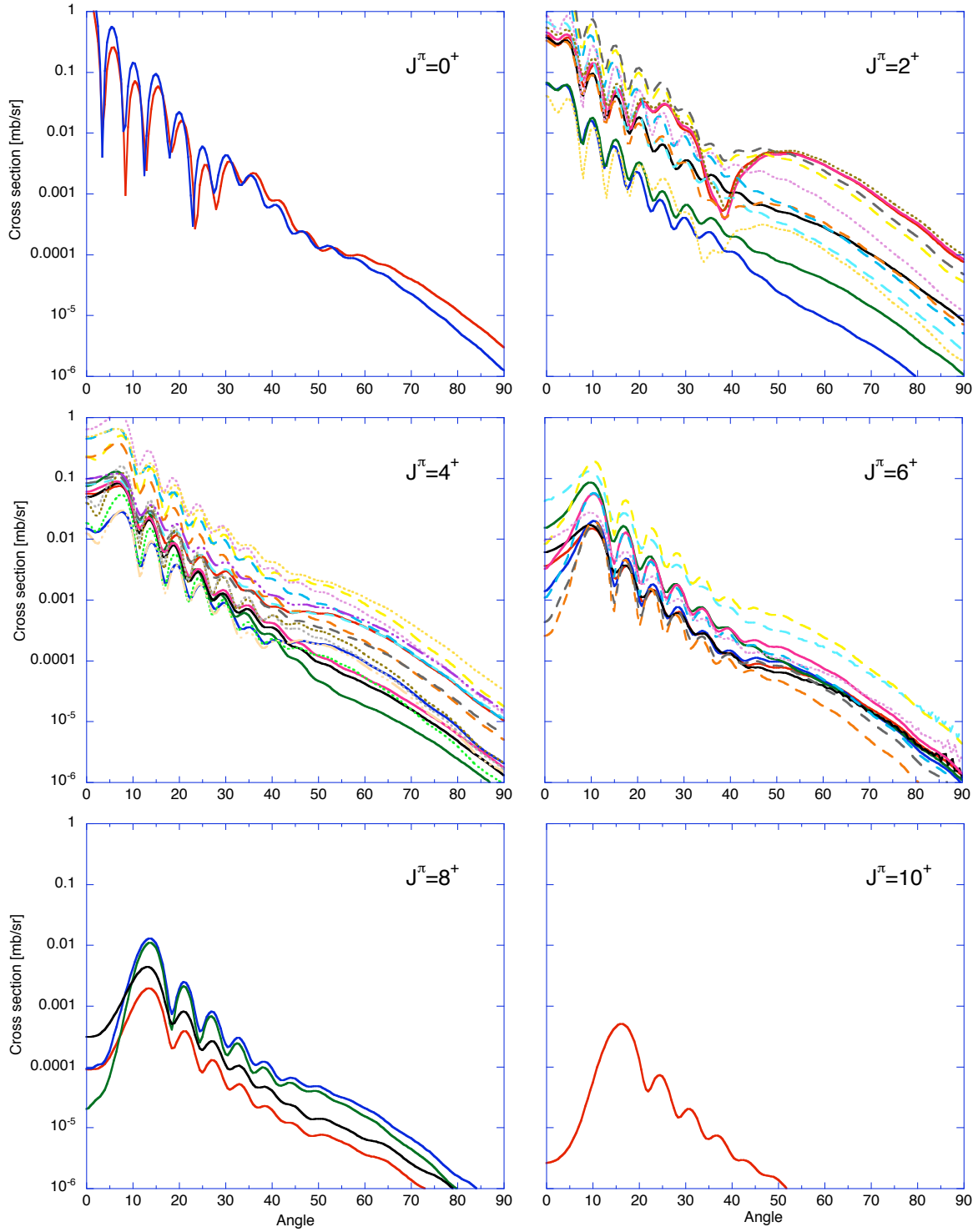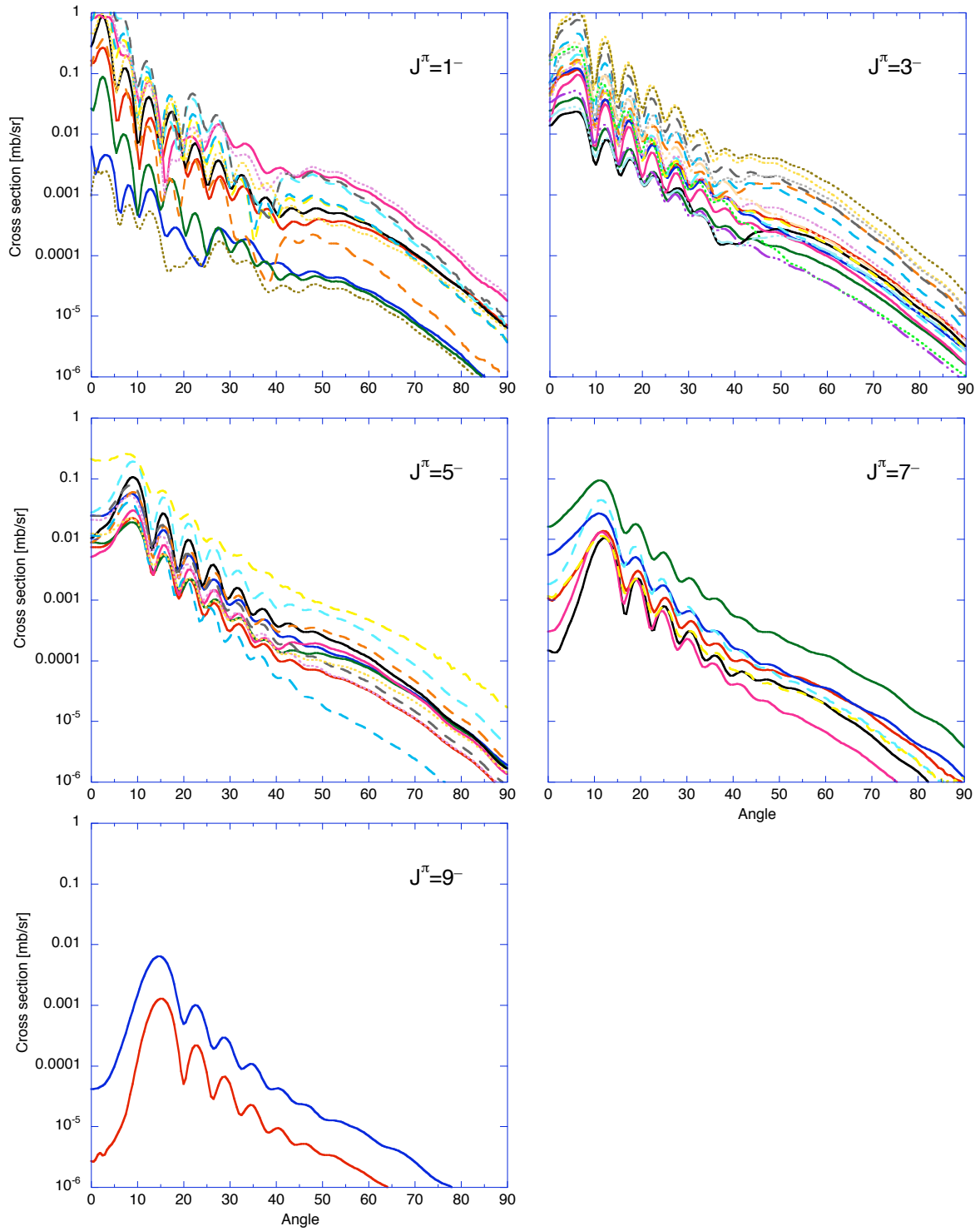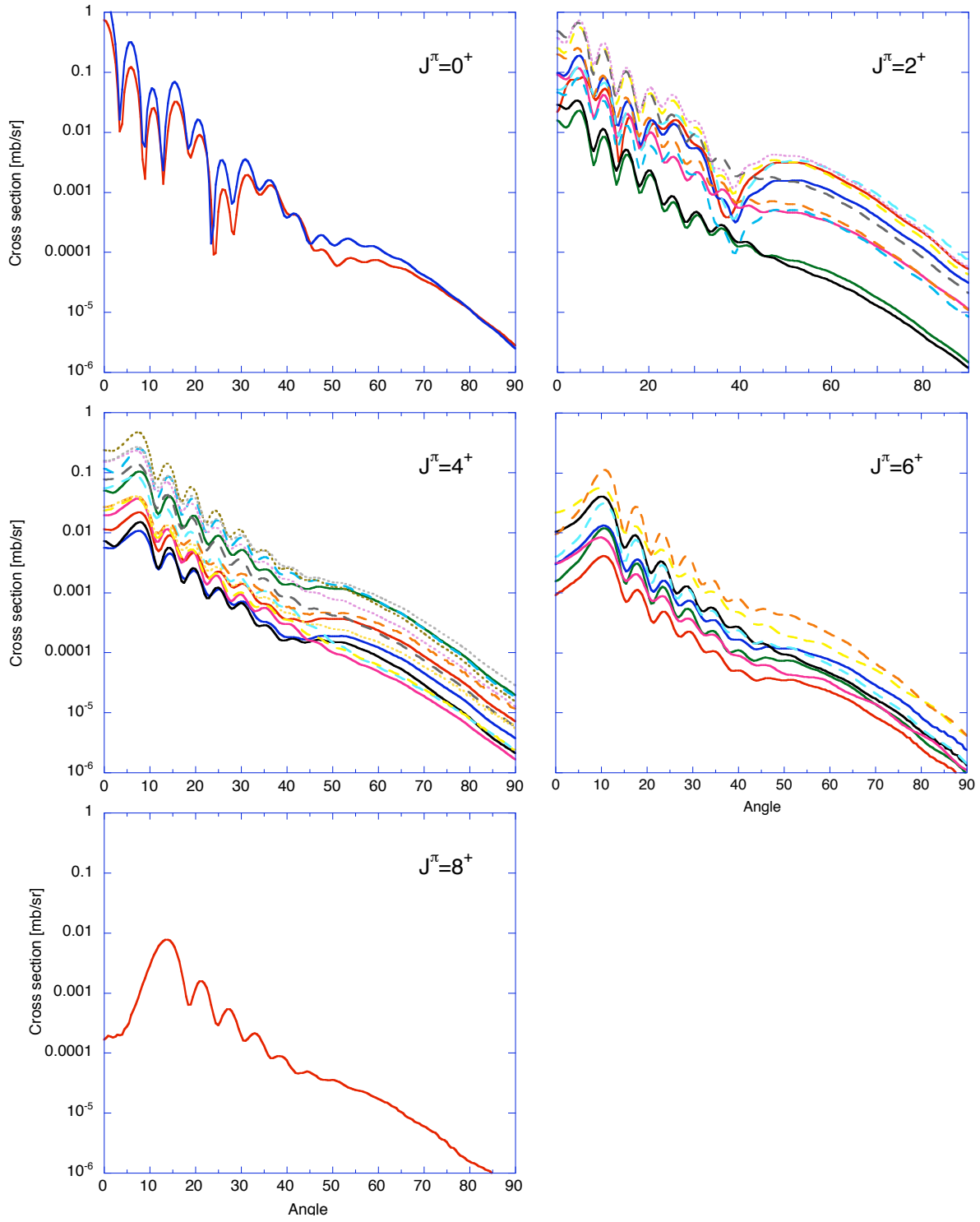
Figure 14: Inelastic scattering cross sections for individual neutron particle-hole excitations. Shown are calculated cross sections for inelastic alpha scattering processes that produce positive-parity excited ^{90}Zr states with a neutron particle-hole structure. The α -^{90}Zr optical potential by Avrigeanu *et al.* (see Sections 5.1-5.2) has been employed for the alpha-core interaction and the Lund parametrization has been used for the alpha-nucleon interaction (see Sections 5.3-5.4).
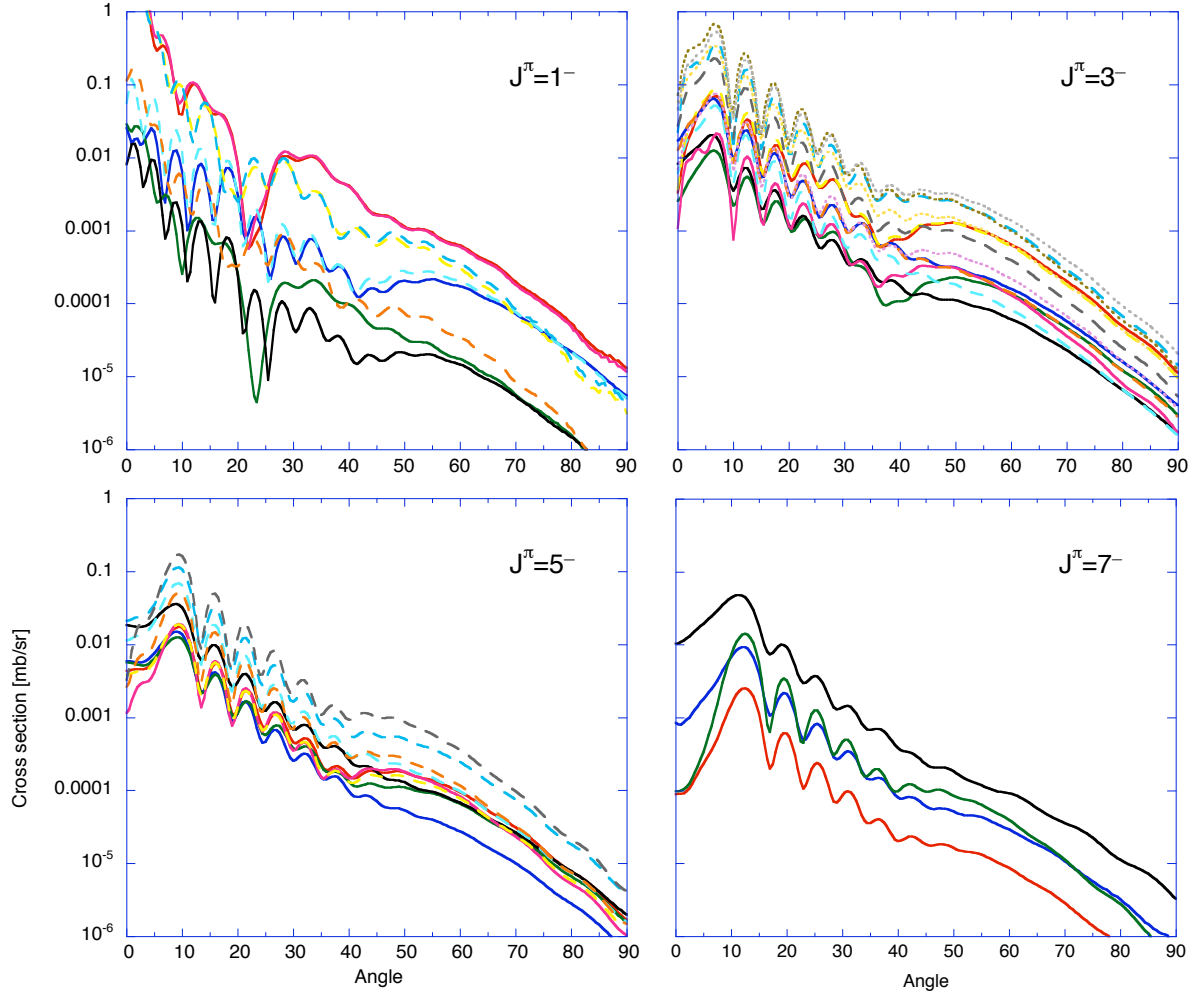
Figure 15: Inelastic scattering cross sections for individual neutron particle-hole excitations. Shown are calculated cross sections for inelastic alpha scattering processes that produce negative-parity excited ^{90}Zr states with a neutron particle-hole structure.

Figure 16: Inelastic scattering cross sections for individual proton particle-hole excitations. Shown are calculated cross sections for inelastic alpha scattering processes that produce positive-parity excited ^{90}Zr states with a proton particle-hole structure.

Figure 17: Inelastic scattering cross sections for individual proton particle-hole excitations. Shown are calculated cross sections for inelastic alpha scattering processes that produce negative-parity excited ^{90}Zr states with a proton particle-hole structure.
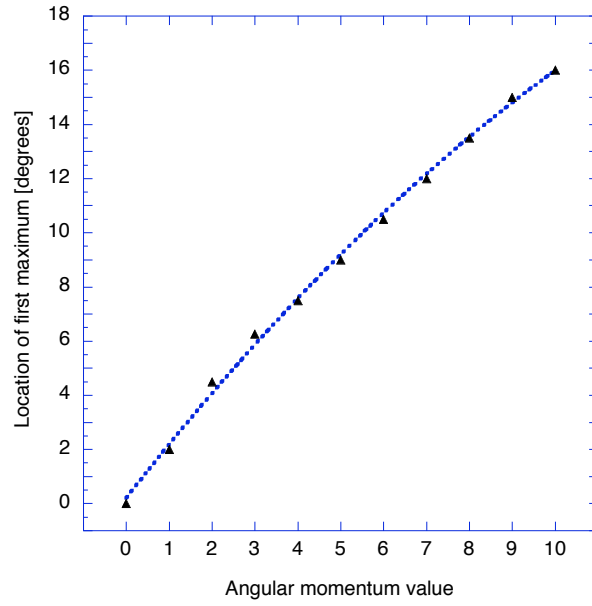
Figure 18: Location of the maxima of the cross section contributions for the various angular-momentum values considered. The curve is drawn to guide the eye.

7 Inelastic Scattering Cross Section for $^{90}\text{Zr}(\alpha, \alpha')^{90}\text{Zr}^*$ at E_α=140 MeV and resulting spin-parity distribution

Combining the energy distributions of the particle-hole states and the cross sections for the individual particle-hole excitations shown in the previous section allows us to determine the $^{90}\text{Zr}(\alpha,\alpha')^{90}\text{Zr}^*$ scattering cross section as a function of the angle of the outgoing α particle. Cross sections can be obtained for producing the excited ^{90}Zr nucleus at a particular excitation energy and for specified values of angular momentum and parity. The sum of the partial cross sections for different $J\pi$ values then gives the total inelastic scattering cross section. While it is rare to find in the literature measured angular distributions for inelastic scattering reactions that produce nuclei above the particle emission threshold, data for inelastic α scattering experiments do exist for ^{90}Zr. Wu *et al.* [77] measured complete energy spectra and angular distributions for the bombardment of ^{27}Al, ^{58}Ni, ^{90}Zr, ^{109}Bi, and ^{232}Th with 140 MeV α particles. They presented results for outgoing p, d, t, ^{3}He, and α particles for angles from 20° to 140°.

7.1 Results

In Figure 19, our calculated inelastic scattering cross section for exciting ^{90}Zr to E_{ex} =10 MeV is compared to experimental cross sections measured by Wu *et al.* [77], as quoted by Bonetti *et al.* [14]. The thick black line in both panels of the figure shows the total inelastic scattering cross section calculated with the model outlined in this report. The contributions from the various $J\pi$ combinations are shown as well. For clarity, contributions from positive and negative parity states have been plotted separately, in the left and right panels, respectively.

For angles in the range of 50° to 90°, we find that the calculated total scattering cross section is in good agreement with the data, while the calculations underestimate the cross section at forward angles by a factor on the order of 5. Note that no error bars are given in Ref. [14]. This level of agreement is not unreasonable for a model that describes the highly-excited ^{90}Zr nucleus in terms of uncorrelated particle-hole excitations. Including many-body correlations, in particular collective effects, will provide a more realistic picture of the scattering process and is expected to improve the agreement.

For the case shown in Figure 19, we find that the largest contributions to the cross section comes from the 1^- and 3^- excitations, followed by contributions from 2^+, 4^+, and 5^- excitations. To show this more clearly, the probablilties for populating different $J\pi$ states are shown in a linear plot in Figure 20, as a function of the scattering angle. The distance between two adjacent curves gives the probability of finding the spin and parity indicated by the values listed at the right end of the upper curve. For example, at 90°, we find about 0% contribution from 0^+ states, 15% from 2^+ states, 8% from 4^+ states, etc. The left panel gives the probabilities obtained by dividing the cross sections for the various $J\pi$ values by the total inelastic scattering cross section. The right panel shows probabilities that have been smoothed in order to account for experimental uncertainties and "binning" in the angular measurements.

We observe that the $J\pi$ distribution is, as expected, angle-dependent, with the largest uncertainties occurring at forward angles ($< 40°$). At larger angles, the probabilities are less sensitive to the angle of the outgoing α particle. Knowing the angular-momentum and parity populations is important for the planning and analysis of Surrogate experiments, since these distributions determine the weights $F(E, J, \pi)$ for the decay probabilities $G_\chi(E, J, \pi)$ that are to be determined or constrained via a measurement of $P_{\delta\chi}$ (see Equation 2 in Section 1). Recent Surrogate experiments detected the outgoing particle at angles between about 40° and 60°. The spin-parity distribution for a particular angle of the outgoing α particle can be obtained by making a cut in Figure 20 at the desired angle. This is illustrated in Figure 22 (left side), where the results of such cuts are shown for 40°, 60°, and 90°. At 60°, for example, the highly excited nucleus is dominated by $J\pi$ =1^- (38%) and 3^- (36%) configurations. Contributions from 2^+ (11%) , 4^+ (6%) , and 5^- (7%) excitations are also important, while larger angular momenta play a minor role.

The calculations can also be carried out for different nuclear excitation energies. Figure 21, e.g., shows the analogous $J\pi$ distributions for an energy of 12 MeV. We find that 2^+ and 4^+ contributions have become more significant at this energy, while the 1^-, 3^-, and 5^- contributions have declined relative to the 10 MeV case. Spin-parity distributions for α angles of 40°, 60°, and 90° are also shown in Figure 22 (right side).

The results found here can be expected to change when additional correlations are included in the calculations. Since collectivity plays an important role in the location of the dipole, quadupole, etc. resonances,

it becomes clear that a more complete picture has to include such many-body correlations. This issue will be investigated in the future. It will be interesting to see the effect of the collectivity not only on the overall cross section, but also on the spin-parity distributions of the excited nucleus.
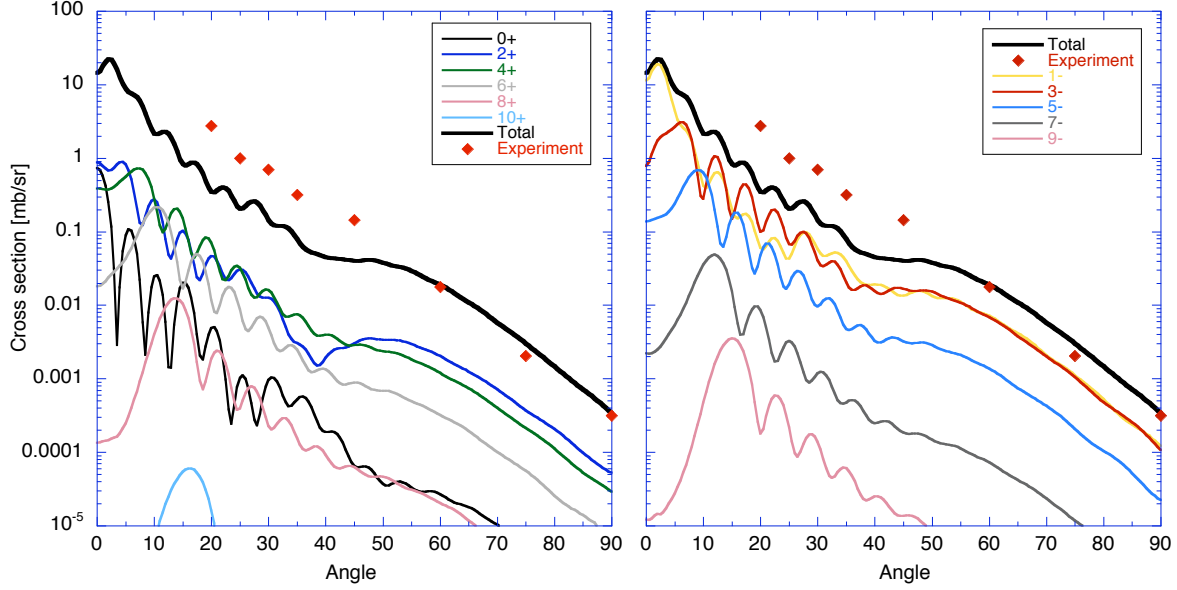

Figure 19: Inelastic scattering cross section for $^{90}\text{Zr}(\alpha, \alpha')^{90}\text{Zr}^*$ with E_α=140 MeV and $E_{\alpha'}$=130 MeV. The total scattering cross section (solid black line) is compared to experimental results (see text). Also shown are the contributions to the scattering cross section that lead to various $J\pi$ states in $^{90}\text{Zr}^*$. Contributions from positive (negative) states are shown on the left (right).
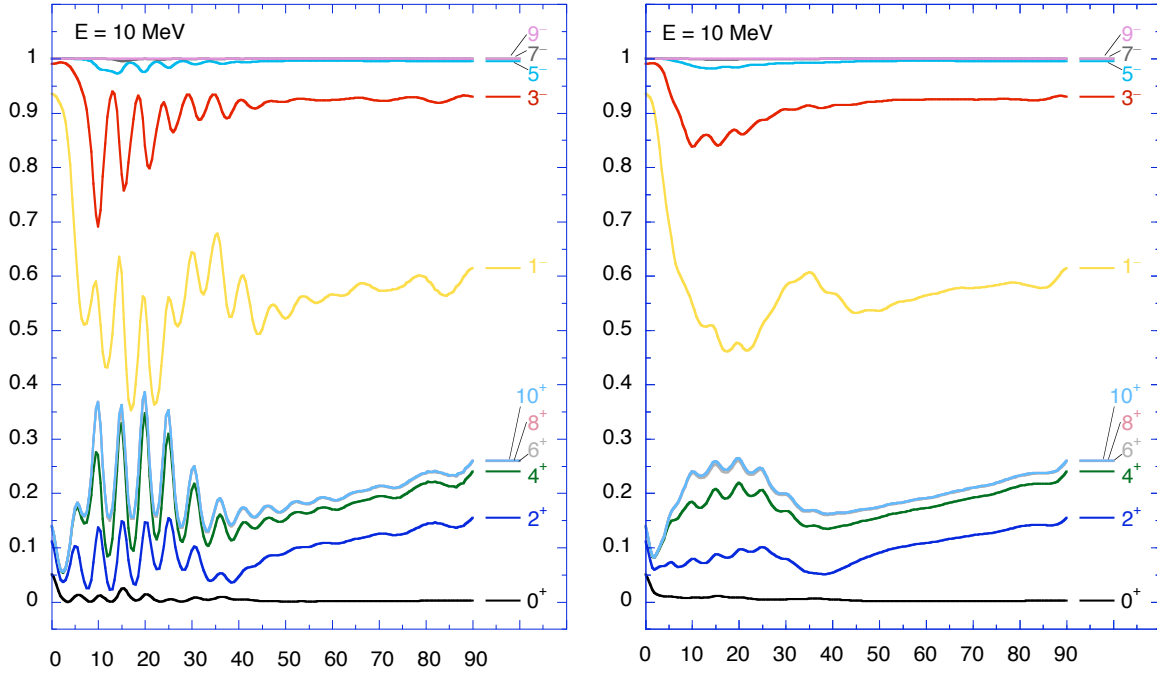
Figure 20: Probabilities for populating various $J\pi$ states in ^{90}Zr* following inelastic alpha scattering with 140 MeV projectiles that leave the target nucleus at excitation energy E_{ex} =10 MeV. The left panel shows the results of the calculation as described in the text, the right panel shows probabilities that have been smoothed in order to account for experimental uncertainties and "binning" in the angular measurements.
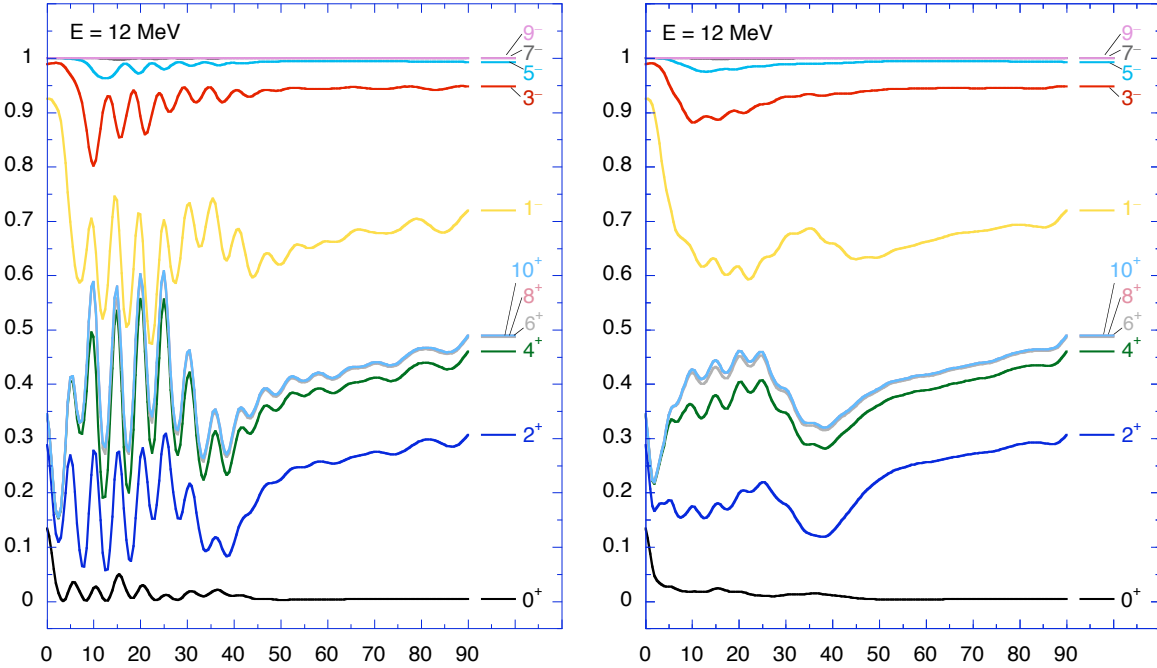

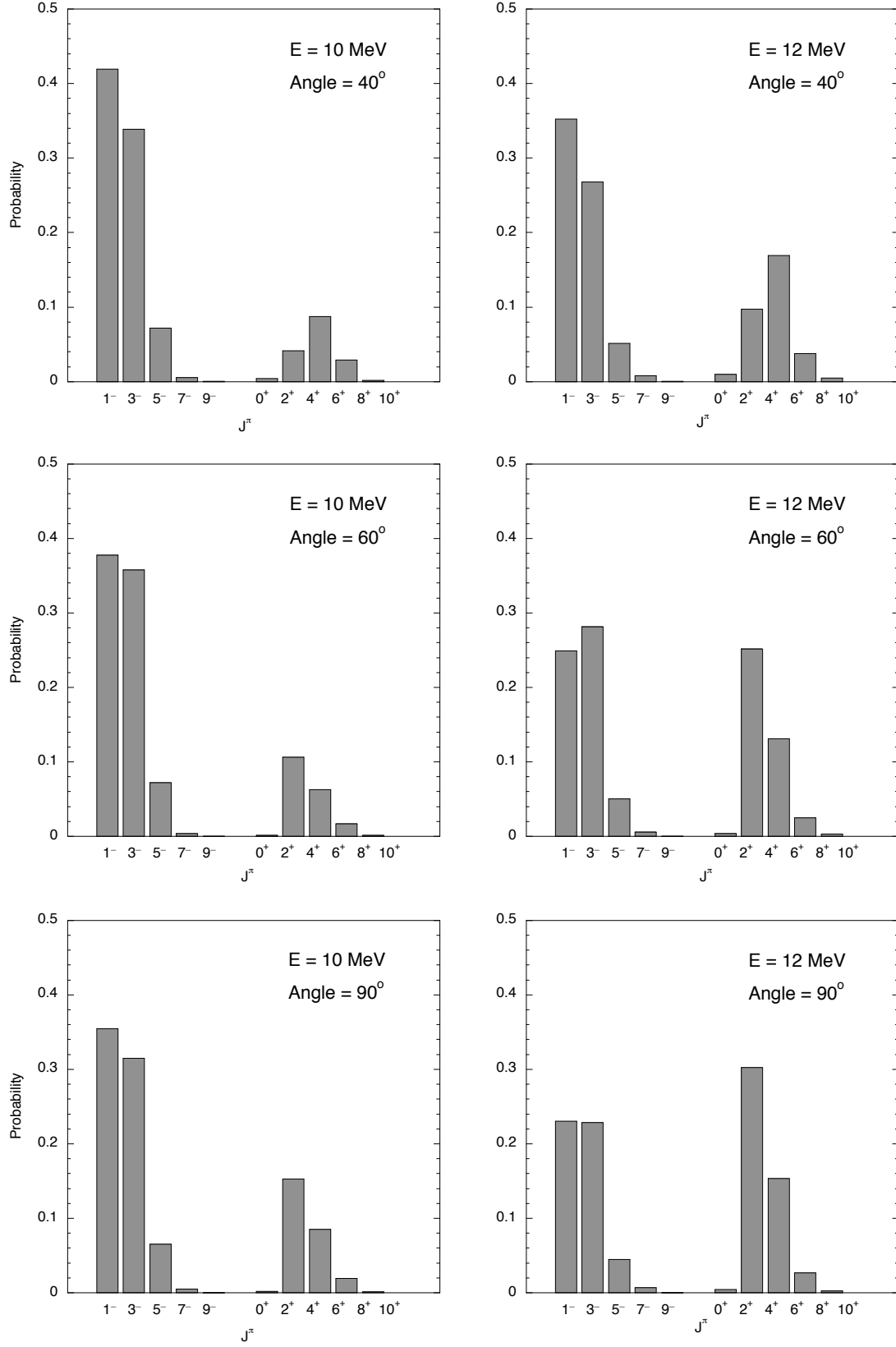Figure 21: Same as in Fig. 20, but for excitation energy E_{ex} =12 MeV.

Figure 22: Spin-parity distributions for ^{90}Zr* at excitation energies E_{ex} =10 MeV (left) and 12 MeV (right), for outgoing α particles at 40°, 60°, and 90°.

8 Summary, Insights, and Recommendations

8.1 Summary of this work

Information on the compound-nuclear $J\pi$ distributions occurring in Surrogate reactions is crucial for testing the validity and limitations of the approximation schemes employed in current analyses of Surrogate experiments, for moving beyond approximate treatments of Surrogate reactions, and for providing reliable estimates of the associated uncertainties in the extracted cross sections.

Providing a proper description of the direct-reaction processes that lead to a compound nucleus in a Surrogate reaction and formulating accurate predictions for the resulting compound-nuclear spin-parity distributions is a nontrivial task. Theoretical descriptions are required for various types of direct reactions that lead to unbound states in spherical, transitional, and well-deformed nuclei, as well as an understanding of the subsequent damping process of the highly-excited intermediate nucleus into a compound system (and the likelihood of particle emission prior to reaching equilibrium). So far, Surrogate experiments have employed one- and two-nucleon transfer (pickup and stripping) reactions, inelastic scattering, and charge exchange reactions.

In this report, a model for predicting the spin-parity distribution in a compound nucleus produced via inelastic α scattering was developed. The focus was on obtaining a first, simple description of the direct-reaction process and on providing the basis for a more complete treatment of the problem. The report specified the approximations made in the present description and identified what a rigorous treatment of the mechanisms that produce a compound nucleus entails.

The model presented here is based on the assumption that the inelastic scattering cross section for a (near-)spherical nucleus can be approximately expressed in terms of cross sections for producing uncorrelated particle-hole excitations in the target nucleus. Specifically, the cross section was given as an incoherent sum of scattering cross sections $(\frac{d\sigma}{d\Omega})_{m_h, m_p}$ for individual particle-hole excitations (m_h, m_p) with weights that depend on the energy and spreading widths of the particle-hole configurations. The spreading (or damping) widths Γ_{m_h, m_p} of the particle-hole excitations arise from their coupling to more complicated (2p-2h, etc.) configurations. It is this coupling that drives the eventual formation of a compound nucleus. The model developed here employed an analytic expression suggested by Brown and Rho [18] for the damping widths. The inelastic scattering cross sections were calculated for each individual particle-hole excitation using the distorted-wave Born-approximation (DWBA) and the coupled-channels code FRESCO [75].

The case considered here involved producing the ^{90}Zr* nucleus at excitation energies of 10 MeV and 12 MeV via inelastic scattering with 140 MeV α projectiles. The cross sections for the individual particle-hole excitations were combined to yield the ^{90}Zr$(\alpha,\alpha')^{90}$Zr* scattering cross section as a function of the angle of the outgoing α particle, and the result was compared to data from inelastic α scattering experiments. For angles in the range of 50° to 90°, we found the calculated total scattering cross section to be in good agreement with the data, while the calculations underestimated the cross section at forward angles by a factor on the order of 5. This level of agreement is not unreasonable for a model that describes the highly-excited ^{90}Zr nucleus in terms of uncorrelated particle-hole excitations. Including many-body correlations, in particular collective effects, will provide a more realistic picture of the scattering process and is expected to improve the agreement.

A prediction for the compound-nucleus spin-parity distributions produced via inelastic scattering was obtained from the calculations described above. The resulting $J\pi$ distribution depends on the angle of the outgoing α particle and exhibits large fluctuations at forward angles ($< 40°$). At larger angles, the probabilities are less sensitive to the angle of the outgoing α particle. Knowing the angular-momentum and parity populations is important for the planning and analysis of Surrogate experiments: These distributions determine the weights $F(E, J, \pi)$ for the decay probabilities $G_\chi(E, J, \pi)$ that are to be extracted from measurements of the coincidence probability $P_{\delta\chi} = \sum_{J,\pi} F_\delta^{CN}(E_{ex}, J, \pi) \; G_\chi^{CN}(E_{ex}, J, \pi)$ and subsequently employed to calculate the desired cross section, $\sigma_{\alpha\chi}(E_a) = \sum_{J,\pi} \sigma_\alpha^{CN}(E_{ex}, J, \pi) \; G_\chi^{CN}(E_{ex}, J, \pi)$ (see Equations 1 and 2).

8.2 Insights and recommendations

The calculations carried out in the simple model presented here exhibit some interesting features that should be studied further: First, the predicted spin-parity distributions show greater sensitivity to the angle of the outgoing α particle than to the excitation energy (for angle and energy variations that typically occur in Surrogate experiments). Second, the predicted $J\pi$ distributions vary rapidly with the angle of the outgoing particle for smaller angles (outgoing particle moving in the forward direction). Since typical experimental analyses group angles into bins, the rapid variations in the forward direction can be expected to lead to a large scatter of the measured coincidence probabilities, unless the Weisskopf-Ewing limit is valid. This prediction could be tested experimentally. If confirmed, this would imply that future Surrogate experiments should be designed in a manner that minimizes the sensitivity to the angle of the outgoing particle.

The model outlined in this report provides a basis for developing a more comprehensive treatment of the process of producing a compound nucleus via inelastic scattering. Scattering from spherical, transitional, and deformed nuclei needs to be studied. Given the simplifying assumptions underlying the model, predictions made in the present framework should be treated as a first estimate and compared against predictions resulting from models of increasing sophistication, as well as experimental findings. In particular:

- The effects of collectivity on the predicted $J\pi$ distributions need to be studied: It is likely that a simple single-particle picture is adequate to describe the spectroscopy of the nuclear configurations reached immediately following a direct reaction of the stripping or pickup reaction type (e.g. (^{3}He,α)) at high excitation energies relevant to Surrogate reactions. However, exciting the nucleus by inelastic scattering (e.g. (p,p') or (α,α')) may require a more complete picture since this type of reaction is highly sensitive to nuclear collectivity. These effects are not included in the uncorrelated particle-hole model employed here. The model can be extended by employing transition potentials in conjunction with a DWBA treatment of the scattering reaction. The transition potentials need to be constructed by convoluting an effective interaction between the projectile and target nucleus with transition densities that contain the relevant correlations.

- The proper description for final states in the continuum needs to be identified: In the context of Surrogate reactions, unbound final states need to be considered (in both inelastic scattering and stripping reactions). The model described here employed a weak-binding approximation for these states. One alternative description, based on the discretized-continuum approach, resulted in large uncertainties in the calculated cross sections (see Sections 3.3 and 3.4). More work is required to adequately address this issue.

- The effects of varying the projectile-target optical potential need to be investigated. An α-nucleus potential obtained via a double-folding procedure should be considered and compared to the phenomenological potential used in the study described here.

- Strictly speaking, the model predicts the $J\pi$ population immediately following the one-step scattering process. The damping that arises from the coupling of the resulting 1p-1h states to more complicated 2p-2h excitations drives the eventual formation of the compound nucleus. Its effect was taken into account schematically by introducing an energy-dependent width for each 1p-1h state and incorporating that width in the summation procedure that yielded the inelastic scattering cross section for excitation to a given final energy and thus the predicted compound nucleus spin-parity distribution. The sensitivity of the calculated cross sections and $J\pi$ distributions to the prescription for determining the widths of the excited states needs to be assessed.

- A more comprehensive treatment of the formation of a compound nucleus via inelastic scattering (or a transfer reaction) would include a detailed, microscopic description of the damping process, as well as width fluctuation effects. Such treatment is beyond the scope of current work.

- Finally, since determining cross sections for n-induced reactions on actinide nuclei is an important goal of the Surrogate research program, the model has to be extended to include the effects of deformation.

Acknowledgments

References

[1] B. L. Andersen, B. B. Back, and J. M. Bang. One-particle transfer reactions to highly excited states in deformed nuclei. *Nucl. Phys. A*, 147:33–44, 1970.

[2] U. Atzrott, P. Mohr, H. Abele, C. Hillenmayer, and G. Staudt. Uniform α-nucleus potential in a wide range of masses and energies. *Phys. Rev. C*, 53(3):1336–1347, Mar 1996.

[3] N. Austern, Y. Iseri, M. Kamimura, M. Kawai, G. Rawitscher, and M. Yahiro. Continuum-discretized coupled-channels calculations for three-body models of deuteron-nucleus reactions. *Phys. Rep.*, 154(3):125–204, October 1987.

[4] V. Avrigeanu, P. E. Hodgson, and M. Avrigeanu. Global optical potentials for emitted alpha particles. *Phys. Rev. C*, 49(4):2136–2141, Apr 1994.

[5] B. B. Back, Ole Hansen, H. C. Britt, and J. D. Garrett. Fission of doubly even actinide nuclei induced by direct reactions. *Phys. Rev. C*, 9(5):1924–1947, May 1974.

[6] C. J. Batty, F. Friedman, and D. F. Jackson. The effective α-nucleon interaction in nuclei. *Nucl. Phys.*, A175:1, 1971.

[7] A. M. Bernstein. Isoscalar transition rates in nuclei from the (α, α') reaction. *Adv. Nucl. Phys.*, 3:325–476, 1969.

[8] L. A. Bernstein, J. Burke, L. Ahle, J. A. Church, J. Escher, et al. Deducing the ^{237}U(n,γ) and (n,2n) cross sections using a new Surrogate Ratio method. *Phys. Rev. C*, page (submitted), 2006. UCRL-TR-xxxxx.

[9] L. A. Bernstein et al. Surrogate nuclear reactions using STARS. In *Proceedings of the International Conference on Nuclear Data for Science and Technology (ND2004, Santa Fe, NM)*, volume 769, pages 890–893. American Institute of Physics, AIP Conference Proceedings, 2005.

[10] F. E. Bertrand, G. R. Satchler, D. J. Horen, J. R. Wu, A. D. Bacher, G. T. Emery, W. P. Jones, D. W. Miller, and A. van der Woude. Giant multipole resonances from inelastic scattering of 152-MeV alpha particles. *Phys. Rev. C*, 22(5):1832–1847, Nov 1980.

[11] G. F. Bertsch. Building a universal nuclear energy density functional. *J. Phys.: Conf. Ser.*, 78:012005, 2007.

[12] G. F. Bertsch, P. F. Bortignon, and R. A. Broglia. Damping of nuclear excitations. *Rev. Mod. Phys.*, 55:287, 1983.

[13] G. F. Bertsch, D. J. Dean, and W. Nazarewicz. Computing atomic nuclei: The Universal Nuclear Energy Density Functional. 2007. (in preparation).

[14] R. Bonetti, L. Colombo, and K.-I. Kubo. Inelastic α-scattering to the continuum: A probe of α-clustering in nuclei. *Nucl. Phys.*, A420:109–123, 1984.

[15] S. Boyer, D. Dassie, J.N. Wilson, M. Aiche, G. Barreau, S. Czajkowski, C. Grosjean, A. Guiral, B. Haas, B. Osmanov, G. Aerts, E. Berthoumieux, F. Gunsing, Ch. Theisen, N. Thiolliere, and L. Perrot. Determination of the ^{233}Pa(n,γ) capture cross section up to neutron energies of 1 MeV using the transfer reaction ^{232}Th(^{3}He,p)^{234}Pa*. *Nucl. Phys. A*, 775:175–187, 2006.

[16] M. G. E. Brand, G. A. Rijsdijk, F. A. Muller, K. Allaart, and W. H. Dickhoff. Fragmentation of single-particle strength and the validity of the shell model. *Nucl. Phys.*, A531:253, 1991.

[17] H. C. Britt and J. B. Wilhelmy. *Nucl. Sci. and Eng.*, 72:222, 1979.

[18] G. E. Brown and M. Rho. *Nucl. Phys.*, A372:397, 1981.

[19] J. Burke, L.A. Bernstein, J. Escher, et al. Deducing the ^{237}U(n,f) cross section using the Surrogate Ratio method. *Phys. Rev. C*, 73:054604, 2006. UCRL-JRNL-217959.

[20] G. Cattapan and E. Maglione. From bound states to resonances: Analytic continuation of the wave function. *Phys. Rev. C*, 61(6):067301, May 2000.

[21] J.A. Church et al. Determining neutron capture cross sections with the surrogate reaction technique: Measuring decay probabilities with STARS. *Nucl. Phys. A*, 758:126c–129c, 2005.

[22] J. D. Cramer and H. C. Britt. *Nucl. Sci. and Eng.*, 41:177, 1970.

[23] J. W. A. den Herder et al. *Nucl. Phys.*, A490:507, 1988.

[24] F. S. Dietrich. Simple derivation of the Hauser-Feshbach and Weisskopf-Ewing formulae, with application to Surrogate reactions. Technical Report UCRL-TR-201718, Lawrence Livermore National Laboratory, Livermore, CA, 2004.

[25] F. S. Dietrich. private communication, 2005.

[26] F. S. Dietrich. Expressions for form factors for inelastic scattering and charge exchange in plane-wave, distorted-wave, and coupled-channels reaction formalisms. Technical Report UCRL-TR-224742, Lawrence Livermore National Laboratory, Livermore, CA, 2006.

[27] G. Duhamel-Chretien, G. Perrin, C. Perrin, V. Comparat, E. Gerlic, S. Gales, and C. P. Massolo. Neutron hole states in ^{89}Zr via the $(\vec{p}, d)$ reaction at 58 MeV. *Phys. Rev. C*, 43:1115, 1991.

[28] J. Escher. Particle-core excitations in inelastic scattering and recoil effects. Manuscript in preparation, 2007.

[29] J. Escher, L. Ahle, L.A. Bernstein, J.A. Church, F. S. Dietrich, C. Forssén, and R. Hoffman. Surrogate nuclear reactions and the origin of the heavy elements. *Nucl. Phys. A*, 758:86c–89c, 2005. UCRL-PROC-205320.

[30] J. Escher and F. S. Dietrich. Determining cross sections for reactions on unstable nuclei: A consideration of indirect approaches. In B. A. Brown, editor, *Second Argonne/MSU/JINA/INT RIA Workshop: Reaction Mechanisms for Rare Isotope Beams*, volume 791, pages 93–100, Melville, New York, 2005. Michigan State University, East Lansing, AIP. UCRL-PROC-212586.

[31] J. Escher and F. S. Dietrich. Indirect methods for nuclear reaction data. In E. Bauge, editor, *Perspectives on Nuclear Data in the Next Decade, Bruyère-le-Châtel, France, September 26–28, 2005*, 2006. UCRL-PROC-217429.

[32] J. Escher, F. S. Dietrich, and M. Dupuis. Independent-particle model versus RPA-based approach to inelastic scattering. Work in progress, 2006.

[33] J. Escher, F. S. Dietrich, and C. Forssén. Surrogate nuclear reaction methods for astrophysics. *Nucl. Instr. and Meth. B*, 261:1075, August 2007. UCRL-JRNL-224284.

[34] J. Escher et al. The Surrogate method - an indirect approach to compound-nucleus reactions. In W. Bauer, R. Bellwied, and S. Panitkin, editors, *Proceedings of the 21st Winter Workshop on Nuclear Dynamics*, pages 49–56, Budapest, Hungary, 2005. Breckenridge, Colorado, February 5–12, 2005, EP Systema.

[35] J. Escher, B. K. Jennings, and H. S. Sherif. Spectroscopic amplitudes and microscopic substructure effects in nucleon capture reactions. *Phys. Rev. C*, 64:065801, 2001.

[36] J. E. Escher and F. S. Dietrich. Examination of the validity of the Surrogate Ratio Method for determining (n,f) and (n,γ) cross sections of actinides. Technical Report UCRL-TR-212509-Draft, Lawrence Livermore National Laboratory, Livermore, CA, 2005.

[37] J. E. Escher and F. S. Dietrich. Surrogate nuclear reactions - an indirect method for determining reaction cross sections. *Jour. Phys. G*, 31:S1687–S1690, 2005. UCRL-JRNL-210888.

[38] J. E. Escher and F. S. Dietrich. Determining (n,f) cross sections for actinide nuclei indirectly: Examination of the Surrogate Ratio Method. *Phys. Rev. C*, 74:054601, 2006. UCRL-JRNL-221555.

[39] J. E. Escher and F. S. Dietrich. Nuclear reaction theory for Surrogate reactions: A progress report for FY07. Technical Report UCRL-TR-234839-Draft, Lawrence Livermore National Laboratory, Livermore, CA, 2007.

[40] G. Finkel, D. Ashery, A. I. Yavin, G. Bruge, and A. Chaumeaux. (^{3}He,d) stripping to unbound analog states in Nb isotopes. *Nucl. Phys.*, A217:197, 1973.

[41] C. Forssén, L. Ahle, L.A. Bernstein, J.A. Church, F.S. Dietrich, J. Escher, and R. Hoffman. Theoretical challenges of determining low-energy neutron capture cross sections via the Surrogate technique. *Nucl. Phys. A*, 758:130c–133c, 2005. UCRL-PROC-205318.

[42] C. Forssén, F.S. Dietrich, J. Escher, V. Gueorguiev, R.D. Hoffman, and K. Kelley. Compound-nuclear reaction cross sections via Surrogate measurements. In *International Symposium on Nuclear Astrophyscs – Nuclei in the Cosmos IX , June 25–30, 2006*, volume Pos(NIC-IX), page 224, 2006. UCRL-PROC-223820.

[43] C. Forssén, F.S. Dietrich, J. Escher, R. Hoffman, and K. Kelley. Determining neutron capture cross sections via the surrogate reaction technique. *Phys. Rev. C*, 75:055807, 2007. UCRL-JRNL-228066.

[44] S. Fortier, S. Gales, S. M. Austin, W. Benenson, G. M. Crawley, C. Djalali, J.S. Winfield, and G. Yoo. One-nucleon-transfer reactions induced by ^{20}Ne at 500 and 600 MeV. *Phys. Rev. C*, 41:2689–2697, 1990.

[45] E. Gadioli and P. E. Hodgson. *Pre-Equilibrium Nuclear Reactions.* Clarendon Press, Oxford, 1992.

[46] N. K. Glendenning. *Direct Nuclear Reactions.* Academic Press, New York, 1983.

[47] Walter Hauser and Herman Feshbach. The inelastic scattering of neutrons. *Phys. Rev.*, 87(2):366–373, Jul 1952.

[48] D. J. Horen, G. R. Satchler, S. A. Fayans, and E.L. Trykov. Microscopic description of the excitation of some states in the ^{90,92,94,96}Zr isotopes. *Nucl. Phys.*, A600:193–235, 1996.

[49] J. P. Jeukenne and C. Mahaux. Shell and space-truncation effects in calculations of the effective mass. *Nucl. Phys.*, A394:445, 1983.

[50] Dao T. Khoa. α-nucleus optical potential in the double-folding model. *Phys. Rev. C*, 63(3):034007, Feb 2001.

[51] A. M. Kobos, B. A. Brown, P. E. Hodgson, G. R. Satchler, and A. Budzanowski. Folding model analysis of α-particle elastic scattering with a semirealistic density-dependent effective interaction. *Nucl. Phys.*, A384:65–87, 1982.

[52] A. M. Kobos, B. A. Brown, R. Lindsay, and G. R. Satchler. Folding model analysis of elastic and inelastic α-particle scattering using a density-dependent force. *Nucl. Phys.*, A425:205–232, 1984.

[53] A. Kolomiets, O. Pochivalov, and S. Shlomo. Microscopic description of excitation of nuclear isoscalar giant resonances by inelastic scattering of 240 MeV α particles. *Phys. Rev. C*, 61(3):034312, Feb 2000.

[54] A. J. Koning and J.-P. Delaroche. Local and global nucleon optical models from 1 keV to 200 MeV. *Nucl. Phys.*, A713:231, 2003.

[55] A. Kumar, S. Kailas, S. Rathi, and K. Mahata. Global alpha-nucleus optical potential. *Nucl. Phys.*, A776:105–117, 2006.

[56] B. J. Lund, N. P. T. Bateman, S. Utku, D. J. Horen, and G. R. Satchler. Isospin character of transitions to the 2_1^+ and 3_1^- states of ^{90,92,94,96}Zr. *Phys. Rev. C*, 51(2):635–650, Feb 1995.

[57] B. F. Lyles, L. A. Bernstein, J. T. Burke, F. S. Dietrich, J. Escher, I. Thompson, D. L. Bleuel, R. M. Clark, P. Fallon, J. Gibelin, A. O. Macchiavelli, M. A. McMahan, L. Phair, E. Rodriguez-Vieitez, M. Wiedeking, C. W. Beausang, S. R. Lesher, B. Darakchieva, and M. Evtimova. Absolute and relative surrogate measurements of the ^{236}U(n,f) cross section as a probe of angular momentum effects. *Physical Review C (Nuclear Physics)*, 76(1):014606, 2007.

[58] B. F. Lyles, L. A. Bernstein, J. T. Burke, F. S. Dietrich, J. Escher, I. Thompson, D. L. Bleuel, R. M. Clark, P. Fallon, J. Gibelin, A. O. Macchiavelli, M. A. McMahan, L. Phair, E. Rodriguez-Vieitez, M. Wiedeking, C. W. Beausang, S. R. Lesher, B. Darakchieva, and M. Evtimova. Publisher's note: Absolute and relative surrogate measurements of the ^{236}U(n,f) cross section as a probe of angular momentum effects [Phys. Rev. C 76, 014606 (2007)]. *Physical Review C (Nuclear Physics)*, 76(1):019905, 2007.

[59] C. Mahaux, P.F. Bortignon, R. A. Broglia, and C.H. Dasso. Dynamics of the shell model. *Phys. Rep.*, 120:1–274, 1985.

[60] V. M. Maslov. ^{237}U neutron-induced fission cross section. *Phys. Rev. C*, 72:44607, 2005.

[61] M. Nolte, H. Machner, and J. Bojowald. Global optical potential for α particles with energies above 80 MeV. *Phys. Rev. C*, 36(4):1312–1316, Oct 1987.

[62] M. Petit, M. Aiche, G. Barreau, et al. Determination of the ^{233}Pa(n, f) reaction cross section from 0.5 to 10 MeV neutron energy using the transfer reaction ^{232}Th(^{3}He, p)^{234}Pa. *Nucl. Phys. A*, 735:347–371, 2004.

[63] C. Plettner et al. Estimation of (n,f) cross sections by measuring reaction probability ratios. *Phys. Rev. C*, 71:051602(R), 2005.

[64] L. W. Put and A. M. J. Paans. Evidence for an energy dependent form factor of the α-particle optical potential. *Phys. Lett.*, 49B:266–268, 1974.

[65] L. W. Put and A. M. J. Paans. The form factor of the real part of the α-nucleus potential studied over a wide energy range. *Nucl. Phys.*, A291:93–125, 1977.

[66] Y. Sakuragi, M. Yahiro, and M. Kamimura. *Prog. Theor. Phys. Suppl.*, 89:211, 1986.

[67] G. R. Satchler. *Direct Nuclear Reactions*. Clarendon Press, Oxford, 1983.

[68] G. R. Satchler. Relation between m_n, m_p and hadronic excitation strenghts when there is strong absorption: The ^{A}Zr(α, α') reactions. *Nucl. Phys.*, A491:413–431, 1989.

[69] G. R. Satchler et al. Isospin and macroscopic models for the excitation of giant resonances and other collective states. *Nucl. Phys.*, A472:215–236, 1987.

[70] G. R. Satchler and Khoa. Missing monopole strength in ^{58}Ni and uncertainties in the analysis of α-particle scattering. *Phys. Rev. C*, 55:285, 1997.

[71] G. R. Satchler and W. G. Love. Folding model potentials from realistic interactions for heavy-ion scattering. *Phys. Rep.*, 55(3):183–254, October 1979.

[72] R. D. Smith and J. Wambach. Damping of the continuum response from 2p-2h excitations. *Phys. Rev. C*, 38:100, 1988.

[73] N. Tanaka, Y. Suzuki, and K. Varga. Exploration of resonances by analytic continuation in the coupling constant. *Phys. Rev. C*, 56(1):562–565, Jul 1997.

[74] N. Tanaka, Y. Suzuki, K. Varga, and R. G. Lovas. Unbound states by analytic continuation in the coupling constant. *Phys. Rev. C*, 59(3):1391–1399, Mar 1999.

[75] I. J. Thompson. Coupled reaction channels calculations in nuclear physics. *Computer Physics Reports*, 7(4):167–212, April 1988.

[76] Y. Wang, C. C. Foster, R. D. Polak, J. Rapaport, and E. J. Stephenson. Proton-^{90}Zr mean field between -60 and +185 MeV from a dispersive optical model analysis. *Phys. Rev. C*, 47:2677, 1993.

[77] J. R. Wu, C. C. Chang, and H. D. Holmgren. Charged particle spectra: 140 MeV α particle bombardment of ^{27}Al, ^{58}Ni, ^{90}Zr, ^{209}Bi, and ^{232}Th. *Phys. Rev. C*, 19(3):659–673, Mar 1979.

[78] W. Younes and H. C. Britt. *Phys. Rev. C*, 67:024610, 2003.

[79] W. Younes and H. C. Britt. *Phys. Rev. C*, 68:034610, 2003.

[80] W. Younes, H. C. Britt, J. A. Becker, and J. B. Wilhelmy. Initial estimate for the ^{237}U(n,f) cross section for $0.1 \leq E_n$ (MeV) ≤ 20. Technical Report UCRL-ID-154194, Lawrence Livermore National Laboratory, Livermore, CA, 2003.